Research Article

Received: 27 February 2022 Revised: 18 April 2022 Accepted article published: 27 April 2022 Published online in Wiley Online Library: 22 May 2022

(wileyonlinelibrary.com) DOI 10.1002/jctb.7098

Adsorptive potential of ZnO/SiO_2 nanorods prepared via the sol–gel method for the removal of Pb(II) and Cd(II) from petroleum refinery wastewater

Elijah Yanda Shaba,* Jimoh Oladejo Tijani, John Olusanya Jacob and Mohammed Abubakar Tanko Suleiman

Abstract

BACKGROUND: The adsorption technique is considered one of the most effective and economical methods for the removal of heavy metals, due to its excellent advantages of low cost, high efficiency and easy handling. This research looks into the possibility of using ZnO/SiO_2 nanorods to remove Cd(II) and Pb(II) from refinery wastewater and their reusability.

RESULTS: ZnO/SiO_2 nanorods were synthesized via the sol–gel method. The analysis of ZnO/SiO_2 shows the formation of a rod-like structure and surface area of 33 $m^2\ g^{-1}$ compared with the 0.3 and 8.620 $m^2\ g^{-1}$ for ZnO and SiO_2, respectively. Effects of adsorption contact time, adsorbent dosage and temperature were examined via batch adsorption. The result indicates that the ZnO/SiO_2 rods exhibited higher adsorption removal efficiency of 85.06% and 84.12% for Pb(II) and Cd(II), respectively, compared to Pb(II) (80.00% and 74.25%) and Cd(II) (76.48% and 70.99%) using ZnO and SiO_2 nanoparticles. A thermodynamic study indicates that the adsorption process was endothermic. The data from the adsorption isotherm were well fitted to the Langmuir isotherm. The pseudo-second-order kinetic model best described the adsorption process. An adsorption–desorption study indicated the adsorption to be concentration-dependent and maintained up to 80.65% and 76.90% for Pb(II) and Cd(II) after the fourth regeneration cycle.

CONCLUSIONS: These findings demonstrated that ZnO/SiO_2 nanorods are a better nanoadsorbent for the removal of Pb(II) and Cd(II) than ZnO and SiO_2 nanoparticles due to their high adsorptive potential and stability.

Supporting information may be found in the online version of this article.

Keywords: adsorption; environmental remediation; environmental chemistry; industrial effluents; kinetics; metals; ZnO/SiO_2 nanorods

ABBREVIATIONS

$\triangle G°$	Standard Gibbs free energy change of adsorption
$\triangle H°$	Standard enthalpy change of adsorption
$\triangle S°$	Standard entropy change of adsorption
$1/n$	Unit of measurement for intensity
b	Constant for Temkin isotherm (g J mol^{-2})
C	Surface adsorption or boundary layer effect
C_e	Equilibrium metal concentration (mg L^{-1})
C_f	Final concentration of heavy metal in refinery wastewater (mg L^{-1})
C_i	Initial concentration of the heavy metal in refinery wastewater (mg L^{-1})
C_o	thesame (mg/L)
k_1	Pseudo-first-order rate constant (min^{-1})
k_2	Pseudo-second-order rate constant (g mg^{-1} min^{-1})
K_d	Distribution coefficient of adsorbate
k_{D-R}	Constant related to adsorption energy
K_F	Constant for Freundlich isotherm
k_{id}	Intraparticle diffusion rate constant (g mg^{-1} min^{-1})
K_L	Constant for Langmuir isotherm (L mg^{-1})
M	Mass of the nanoadsorbent (g)
q_e	Mass of metal adsorbed at equilibrium
q_{max}	Maximum adsorption capacity (mg g^{-1})
q_t	Mass of metal adsorbed at any time t
R	Gas constant (8.314 J K^{-1})
T	Temperature (K)
V	Volume of refinery wastewater (L)
α	Initial adsorption rate (mg g^{-1} min^{-1})
β	Constant for desorption (g mg^{-1})
ε	Polanyi potential

* *Correspondence to: EY Shaba, Department of Chemistry, Federal University of Technology, PMB 65, Minna, Niger State, Nigeria. E-mail: elijah.shaba@futminna.edu.ng*

Department of Chemistry, Federal University of Technology, Minna, Niger State, Nigeria

INTRODUCTION

The growing human global population and demand–supply chain for petroleum products coupled with the expansion of petrochemical industries have led to the increasing release of refinery wastewater into the environment.[1] The direct discharge of untreated petroleum wastewater has contaminated surface and groundwater resources with petrochemical products and consequently poses a significant risk to human health as well as animal life.[2,3] It has been reported that *ca* 3500–5000 L of petroleum wastewater are generated per tonne of crude oil processed. The wastewater generated from petrochemical industries contains several heavy metals such as vanadium, copper, cadmium, selenium, chromium, iron, lead and nickel, among others.[4] It has been reported that lead causes negative effects on humans which include nausea, vomiting, abdominal pain, renal failure, hallucinations, mental retardation, birth defects, dyslexia, psychosis, paralysis, muscle weakness, weight loss, brain damage and kidney damage, and even death can occur as a result of chronic lead exposure.[5,6] Cadmium is also known to cause stomach irritation, vomiting, fragile bones, kidney, lung damage, genetic disorders and interruption in hormone secretions.[7] These heavy metals are mobile, sometimes pseudo-persistent, non-biodegradable and highly recalcitrant in the environment and as such are difficult to remove using conventional wastewater processes. Thus, effective removal of these undesirable elements is very necessary for a sustainable ecosystem.

Various conventional methods have been studied for wastewater treatment, which include: biological processes,[8] flocculation, precipitation, co-precipitation, electrolysis and membrane processes,[9] ion exchange, coagulation and adsorption[10] to mention but a few. However, among all these techniques, adsorption is considered the best and most cost-effective technique for wastewater treatment, because of its excellent advantages of availability, high efficiency at a reasonable cost and easy handling.[11] Due to the aforementioned advantages, extensive research has been done on the development of adsorbents such as activated carbons, polymer materials, zeolites, biofuels and industrial byproducts for the elimination of heavy metals.[12] However, these adsorbents have significant drawbacks which include limited loading capacities, low selectivity, few metal ion binding sites and low economic feasibility.[13] In light of these setbacks, researchers have focused on the development of nanoadsorbents for the elimination of pollutants from petrochemical wastewater. Efforts have been made to produce nanoabsobents of different sizes, morphologies and shapes, with high compatibility and stability,[14] via various synthesis methods including hydrothermal, ball milling method, thermal decomposition, biological and green methods, co-precipitation, sol–gel and microemulsion methods.[15] Among these methods, the sol–gel method is a versatile and effective approach because of its simplicity and versatility, low-temperature synthesis, cost-effectiveness and production of a very fine powder. Additionally, in comparison to other synthesis methods, it allows for more control over other processes.[16] Various nanoadsorbents (metal oxides) such as manganese, ferric, titanium, aluminium, selenium, zinc and silicon oxide nanoparticles have been produced for the removal of heavy metals from industrial wastewater.[17] Metal oxides, such as ZnO, have long been recognized as viable nanoadsorbents, due to their unique characteristics such as excellent electron mobility, superior transparency and strong room-temperature luminescence.[18] Angelin *et al.*[19] used spherical ZnO nanoparticles (8 nm) produced via the sol–gel process as an adsorbent for Hg(II), Pb(II), Bi(III) and Cd(II) removal under reaction conditions of time (60 min), dose (0.250 g), temperature (30 °C) and metal ion concentration of 0.01 mol L^{-1}. The removal values for Hg(II), Pb(II), Bi(III) and Cd(II) reported were 86.8%, 97.1%, 61.2% and 80.9%, respectively. Kamath *et al.*[20] successfully synthesized ZnO nanorods for Cr(VI) removal. Those authors reported 0.00165 mg g^{-1} to be the highest adsorption capacity. On the contrary, ZnO nanoparticles have drawbacks of stability in an aqueous matrix. Recently, attention has shifted to the synthesis of hybrid nanocomposites with improved properties that pure nanoparticles could not attain on their own. For example, the potential of polypyrrole/ZnO nanocomposites for the removal of Pb(II) (92.1%) and Cd(II) (84.6%) ions has been studied. The highest removal efficiencies of Cd(II) and Pb(II) ions were reported by those authors at a dosage of 1 g, contact duration of 50 min and pH of 6.[21] Similarly, Tho *et al.*[22] used cassava root husk-derived biochar to immobilize As(III), Pb(II), Cd(II) and Cr (VI) ions from ZnO nanoparticles, with maximum adsorption capacities of 39.52, 44.27, 42.05 and 28.37 mg g^{-1}, respectively.

Silica (SiO_2) nanoparticles have several distinct advantages as a delivery vehicle, including great biocompatibility, high hydrophobicity, thermal stability, high flexibility and pH change resistance, as well as a high degree of multifunctionality.[23] Many researchers have used SiO_2 nanoparticles to remove heavy metals, including Sheet *et al.*,[24] who examined the removal of lead, chromium, cadmium, zinc and nickel ions using SiO_2 nanoparticles as an adsorbent. Those authors reported the removal amounts to be 85.60%, 85.0%, 88.33%, 63.0% and 89.90% for zinc, lead, chromium, cadmium and nickel, respectively, at a contact time of 60 min using 20 mg per 20 cm^3 of heavy metal solutions of pH 3.

To improve the performance of adsorbents in removing heavy metals from wastewater, researchers have now focused on the production of hybrid nanocomposites.[10] Heavy metals have been removed from wastewater using a variety of hybrid nanocomposites. As an example, Soltani *et al.*[25] synthesized ZnO/SiO_2 nanocomposites by a wet impregnation method for photocatalytic degradation of a textile dye. Similarly, flower-like ZnO/SiO_2 nanocomposites were synthesized via the hydrothermal method by Babu *et al.*[26] for photocatalysis and antibacterial applications. Nevertheless, no work has been performed that specifically investigated ZnO/SiO_2 nanorods with good environmental stability, ease of preparation and compatibility with other materials for Pb(II) and Cd(II) removal from refinery wastewater.

Despite the success in the use of nanomaterials for the removal of pollutants from wastewater, the discharge of adsorbents that have been exhausted is a serious environmental issue.[27] As a result, it is critical to regenerate and reuse adsorbents to make the adsorption process economically and environmentally friendly. Desorption and reutilization of spent adsorbents in adsorption–desorption cycles may significantly minimize the discharge of the spent adsorbent into the environment. Desorption can be achieved through thermal (solvent-free) and solvent methods. The solvent desorption method is known to be environmentally friendly, inexpensive, quick, promising and has a lot of potential.[28]

From previous literature, the SiO_2 nanoparticles used were synthesized from chemical sources which are costly and generate secondary pollutants. The SiO_2 nanoparticles used in the study reported here were synthesized from naturally available kaolin to reduce cost. Additionally, much research used simulated waste-

water for the adsorption process. The objectives of the work reported here were to synthesize and characterize ZnO/SiO_2 nanorods and to study their adsorption potential as a nanoadsorbent for the elimination of Pd(II) and Cd(II) from real petroleum refinery wastewater and their reusability. Effects of parameters such as adsorbent dosage, temperature and contact time on the removal efficiency of the target heavy metals ions from refinery wastewater using the ZnO/SiO_2 nanorods were examined. The experimental data were evaluated using the Elovich model, intraparticle diffusion model and pseudo-first- and pseudo-second-order models. Adsorption isotherms were investigated, and several isotherm models, such as the Langmuir, Freundlich and Dubinin–Radushkevish (D-R) models, were tested. In addition, to investigate the mechanism during the adsorption process, thermodynamic properties such as standard enthalpy change ($\Delta H°$), standard entropy change ($\Delta S°$) and standard free energy change ($\Delta G°$) were analyzed.

MATERIALS AND METHODS

Sigma Aldrich provided analytical-grade sodium hydroxide (NaOH) and polyvinylpyrrolidone (PVP) with purity levels ranging from 90% to 95%. All chemicals were utilized without being purified in any way. Raw kaolin was collected from Pati Shabakolo in the Lavun local government area of Niger State. The petrochemical effluent from Kaduna refineries was collected in January 2018.

Kaolin pretreatment

Using a mortar and pestle, kaolin was disaggregated. A 75 μm mesh sieve was used to sieve the crushed kaolin. To make a slurry, a known quantity (400 g) of crushed kaolin was soaked in 1000 cm^3 of distilled water for a week. The supernatant was decanted until the distilled water became colorless and the slurry was dried (overnight) at 100 °C.

Metakaolinization

Meatakaolinization of the Pati Shabakolo kaolin was carried out by calcination of 20 g of the treated kaolin (800 °C) in a muffle furnace for 2 h.

Synthesis of ZnO/SiO_2 nanorods

Firstly, ZnO nanoparticles were prepared by measuring 60 cm^3 of a known concentration of zinc nitrate (0.1 mol L^{-1}) into a 250 cm^3 beaker, which was placed on a magnetic stirrer. An amount of 25 cm^3 of 1.0 mol L^{-1} NaOH solution was slowly added. After which, 10 cm^3 of 5% (w/v) PVP solution was added to the same mixture. This was accompanied by the formation of a gel-like solution. The gel solution was aged overnight before being dried in an oven (100 °C) for 2 h and then calcined (450 °C) for 2 h. Secondly, SiO_2 nanoparticles were prepared by measuring 100 cm^3 of 2 mol L^{-1} NaOH into 250 cm^3 conical flasks followed by the addition of 1.5 g of metakaolin. To achieve a homogeneous solution, the solution was vigorously agitated for 2 h at 2000 rpm on a magnetic stirrer (model 400) and then left to age overnight. Each sample was washed thoroughly using distilled water to get a neutral pH (7) after crystallization. The obtained sample was calcined at 200 °C overnight. Furthermore, the sol–gel method was followed to synthesize the ZnO/SiO_2 nanorods by measuring 0.1 mol L^{-1} zinc nitrate into a 250 cm^3 beaker placed on a magnetic stirrer followed by the addition of 1.5 g of metakaolin. To get a homogenous solution, the solution was vigorously stirred at 2000 rpm on a magnetic stirrer for 2 h. The resulting solution was vigorously stirred for 30 min with a mechanical shaker and allowed to age for 24 h. The resulting ZnO/SiO_2 nanorods were calcined (450 °C) for 2 h.[29]

Characterization of nanocomposites

Characterization of ZnO and SiO_2 nanoparticles and ZnO/SiO_2 nanorods was carried out to determine their mineralogical phases, morphology, elemental compositions, functional groups, chemical states and surface area using high-resolution scanning electron microscopy (HRSEM; MEL-300000), X-ray diffraction (XRD; XRD-60000), energy-dispersive spectroscopy (EDS), X-ray photoelectron spectroscopy (XPS; XPSHI 5400), Brunauer–Emmett–Teller (BET) N_2 adsorption–desorption measurements and Fourier transform infrared (FTIR) spectroscopy (Frontier FTI-R).

Collection and preparation of refinery wastewater

Wastewater was collected from the Kaduna petrochemical refinery. To keep the oxidation states of the various elements in the solution stable and prevent precipitation, the refinery wastewater collected was treated with dilute nitric acid. The sample was taken to a laboratory as soon as possible for digestion.

Determination of heavy metal concentrations of refinery wastewater

About 50 cm^3 of refinery wastewater was digested at 80 °C with 10 cm^3 of concentrated HNO_3 until the volume reached 20 cm^3, then cooled and filtered.[30] The clear solution was diluted to a mark of 100 cm^3 with distilled water, and blank digestion was performed in the same manner. Except for the wastewater, the blank solution contained all of the reagents. Triplicates of each sample were digested. The digests were tested for Pb(II) and Cd(II) using a flame atomic absorption spectrophotometry (AAS) instrument (AASPG 990).

Batch adsorption experiments

Effect of contact time

The removal of Pb(II) and Cd(II) from the refinery wastewater using ZnO and SiO_2 nanoparticles and ZnO/SiO_2 nanorods as adsorbents was studied. A known volume of the refinery wastewater (50 cm^3) was measured into separate conical flasks. The conical flasks were corked and the solution was stirred continuously at 250 rpm for various contact times (1, 5, 10, 15, 20 and 25 min) at 30 °C and adsorbent dosage of 0.08 g of ZnO, SiO_2 and ZnO/SiO_2 nanorods. The liquid phases were filtered out of the solution at the end of each mixing interval and the residual concentrations of Pb(II) and Cd(II) were determined using AAS.[31]

Effect of nanoadsorbent dosage

The removal of Pb(II) and Cd(II) from the refinery wastewater was studied at different adsorbent dosages of 0.02, 0.04, 0.06, 0.08, 0.1 and 0.12 g per 50 cm^3 using separate conical flasks. The conical flasks were corked and the solution was stirred continuously at 250 rpm for 15 min. The liquid phases were filtered out of the solution at the end of each mixing interval and the residual concentrations of Pb(II) and Cd(II) were determined using AAS.[31]

Effect of reaction temperature

The removal of Pb(II) and Cd(II) from the refinery wastewater was studied at different temperatures (30, 40, 50, 60, 70 and 80 °C) regulated by a thermostat attached to a shaker. A known volume of the refinery wastewater (50 cm^3) was measured into separate conical flasks. The conical flasks were corked and the solution was

stirred continuously at 250 rpm. Dosage and contact time were kept constant at 0.08 g and 15 min, respectively. The liquid phases were filtered out of the solution at the end of each mixing interval and the residual concentrations of Pb(II) and Cd(II) were determined using AAS.[31]

Desorption experiments

Desorption studies were performed using 0.025, 0.08 and 0.1 mol dm^{-3} HNO_3 solutions. Nanocomposites previously exposed to the petroleum refinery wastewater were extracted from the solution and mixed with 20 cm^3 of HNO_3 solution. Agitation was performed using an orbiter shaker for 15 min.

The concentration of heavy metals was measured. The desorption efficiency was calculated using the following formula:

$$\text{Desorption efficiency}(\%) = \frac{\text{released pollutant concentration}}{\text{initially sorbed concentration of pollutant}} \times 100 \quad (1)$$

Reusability

To determine the reusability of ZnO and SiO_2 nanoparticles and ZnO/SiO_2 nanocomposites, an adsorption–desorption cycle was repeated four times using the same sample. Desorption studies were performed using 0.1 mol dm^{-3} HNO_3 solutions. ZnO and SiO_2 nanoparticles and ZnO/SiO_2 nanocomposites previously exposed to the refinery wastewater were extracted from the solution and mixed with 20 cm^3 of HNO_3 solution. Agitation was performed using an orbiter shaker for 15 min. The desorbed ZnO and SiO_2 nanoparticles and ZnO/SiO_2 nanocomposites were used for the removal of heavy metals from the refinery wastewater by measuring 0.05 g of the desorbed nanocomposites into conical flasks containing 50 cm^3 of petroleum wastewater. The conical flasks were corked and the mixture was stirred continuously on a magnetic stirrer at 250 rpm for 15 min at 30 °C and pH of 6.25. The liquid phases were separated from the solution by filtration with Whatman filter paper No. 4 at the end of each mixing period, and the equilibrium concentrations of Pb(II) and Cd(II) were determined using AAS.[32]

Data analysis

The equilibrium adsorption capacity and the removal of Pb(II) and Cd(II) ions were calculated using Eqns (2) and (3):

$$q_e = \frac{(C_i - C_f) \times V}{m} \quad (2)$$

$$\text{Adsorption}\,(\%) = \frac{C_i - C_f}{C_i} \times 100 \quad (3)$$

Pseudo-first-order model

According to the pseudo-first-order kinetic model, adsorption takes place entirely on isolated sites, and there is no interaction between the adsorbed ions.[33] The adsorption rate is proportional to the number of vacant sites. The pseudo-first-order kinetic model equation is as follows:

$$\log(q_e - q_t) = \log(q_e) - \frac{K_1}{2.303} \times t \quad (4)$$

The values of K_1 and q_e are determined from the slope and intercept, respectively, of a plot of $\log(q_e - q_t)$ *versus* t.

Pseudo-second-order model

Ho and McKay were the first to describe the pseudo-second-order model for the kinetic process of divalent metal ion adsorption on an adsorbent. The pseudo-second-order model implies that chemical adsorption is the rate-determining step and predicts behavior across the whole adsorption range.[34] In this case, the adsorption rate is determined by the adsorption capacity.[35] The pseudo-second-order equation is as follows:

$$\frac{t}{q_t} = \frac{1}{k_2 {q_e}^2} + \frac{t}{q_e} \quad (5)$$

The slope and the intercept of a plot of t/q_t *versus* t were used to determine the values of q_e and k_2.

Intraparticle diffusion model

Weber and Morris proposed and developed the intraparticle diffusion model, which takes pore diffusion into account. Intraparticle diffusion is assumed to be the slowest stage during the adsorption process.[36] As a result, the rate-controlling step is determined with instantaneous adsorption in the internal diffusion model. The equation for the adsorption system is given by Weber and Morris[37] as follows:

$$q_t = k_i t^{0.5} + C \quad (6)$$

Elovich model

The Elovich model[38] can be used to understand the nature of adsorption. This model aids in the prediction of a system's mass and surface diffusion, as well as activation and deactivation energy.[39] Although the model was originally designed for gaseous systems, it is useful in predicting the nature of adsorption in wastewater processes. The Elovich model assumes that as the amount of adsorbed solute increases, the rate of adsorption decreases exponentially. The Elovich equation is as follows:

$$q_t = \frac{1}{\beta}\ln\alpha\beta - \frac{1}{\beta}\ln(t) \quad (7)$$

Adsorption isotherms

Adsorption isotherms give basic physiochemical data for determining the adsorption process applicability as a unit operation. The adsorption between metal ions and nanocomposites was studied using the Langmuir, D-R, Freundlich and Temkin models. The Freundlich model considers heterogeneous adsorption, whereas the Langmuir model considers monolayer adsorption with constant adsorption energy.[40] According to the Temkin isotherm model, as the adsorbed layer's coverage increases, the heat of adsorption decreases. The D-R isotherm is an isotherm that can be applied to both homogeneous and heterogeneous surfaces to characterize adsorption. The Langmuir, Freundlich, Temkin and D-R equations are presented in Table 1.

Note that the separation factor R_L (dimensionless) is defined by the following equation:

$$R_L = \frac{1}{1 + K_L C_e} \quad (12)$$

RESULTS AND DISCUSSION

HRSEM analysis of ZnO, SiO_2 and ZnO/SiO_2 nanorods

The morphologies of ZnO and SiO_2 nanoparticles and ZnO/SiO_2 nanorods were studied using HRSEM. Their corresponding micrographs are displayed in Fig. 1.

Figure 1(a) shows an agglomerated homogeneously distributed spherical shape. Figure 1(b) indicates the formation of a mixture of well-agglomerated spherical and hexagonal shapes. There is a morphological transformation from spherical shape and irregular hexagonal shape obtained for ZnO and SiO_2 to a rod-like shape, as shown in Fig. 1(c). The transformation to the rod-like structure can be attributed to the establishment of oxide clusters of Si–O–Zn based on the diffusion of the smaller Si ions with an ionic radius of 0.4 Å on the lattice of Zn ions with a larger ionic radius (0.74 Å) in the hexagonal wurtzite structure of the ZnO nanoparticles. This indicates the formation of new material different from the SiO_2 and ZnO nanoparticles, evidence of the electrostatic force of attraction between the particles.[41] Different morphologies have been reported by Widiyastuti *e al.*[42] Those authors reported the transformation from rod-like ZnO nanoparticles to flower-like morphology after the addition of SiO_2 nanoparticles. Additionally, the flower-like morphology of ZnO/SiO_2 has also been reported.[26] The difference in this analysis could be because of the synthesis method of ZnO and SiO_2 nanoparticles and the ZnO/SiO_2 nanorods.

Table 1. Equations of adsorption for Langmuir, Freundlich, Temkin and D-R isotherms

Isotherm	Equation
Langmuir	$\frac{C_e}{q_e}=\frac{1}{q_{max}K_L}+\frac{C_e}{q_{max}}$ (8)
Freundlich	$\log q=\log K_f+\frac{1}{n}\log C$ (9)
Temkin	$q_e=\frac{RT}{b}\ln K_T+\frac{RT}{b}\ln C_e$ (10)
R-D	$\ln q_e=\ln q_m-K_{D-R}\varepsilon^2$ (11)

Elemental analysis of ZnO, SiO_2 and ZnO/SiO_2 nanorods

EDS was used to conduct elemental analysis of synthesized SiO_2, ZnO and ZnO/SiO_2 nanorods. The spectra are presented in Fig. 2.

The EDS trace in Fig. 2(c) indicates that the synthesized ZnO/-SiO_2 nanorods primarily contain Si, Zn and O elements. In both Figs 2(a) and (b), the peak of O appears at 0.57 keV, the peaks of

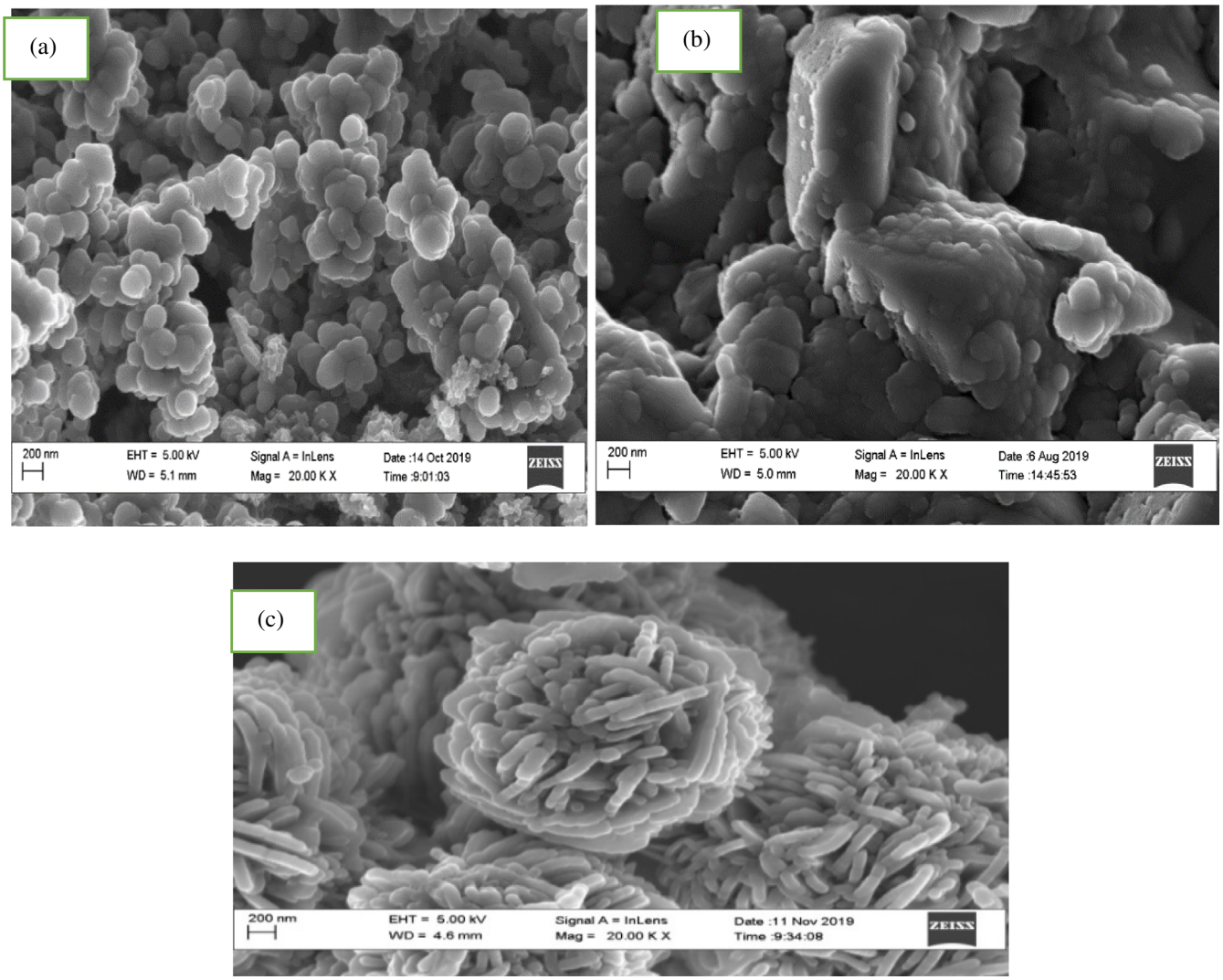

Figure 1. HRSEM images of (a) ZnO, (b) SiO_2 and (c) ZnO/SiO_2 nanorods.

Zn appear at 1.08, 8.75 and 9.68 keV, and the peak of Si appears at 1.75 keV. The values obtained for the ZnO/SiO_2 nanorods show an increase in binding energy for O, Zn and Si, which is because of the diffusion of Si ions into the interstitial spaces between Zn^{2+} and O^{2-} ions. The atomic percentage was found to be 19.59, 45.49 and 34.91 wt% for Zn, Si and O, respectively. This result corroborated the XRD analysis (discussed later) with SiO_2 dominance.

FTIR spectroscopy

FTIR spectroscopy was used to analyze the functional groups in ZnO and SiO_2 nanoparticles and ZnO/SiO_2 nanorods. The results are shown in Fig. 3.

Figure 3(a) shows a typical FTIR spectrum of SiO_2 nanoparticles in the range 500–4000 cm^{-1}. The peaks at 793 and 1020 cm^{-1} correspond to the asymmetric vibration mode and symmetric stretching mode of the SiO_2 groups (O—Si—O), respectively. This result is similar to that of the absorption band reported by Abello-Ribota *et al.*[43] The peak at 950 cm^{-1} is attributed to the presence of asymmetric vibration of Si—H bond. The presence of a peak at 1640 cm^{-1} is attributed to bending of O—H groups of SiO_2 (H bonding) of adsorbed water which is based on the scissor bending vibration of water molecules.[44] The presence of these functional groups may be beneficial in the application of SiO_2 nanoparticles in wastewater treatment. Other researchers[45,46] have independently reported similar results. The FTIR spectrum in Fig. 3(b) shows a stretching vibration of C═O at 1735 cm^{-1}.[47] The absorption band at 1358 cm^{-1} is due to the presence of the C—H bond.[48] The C—N stretching vibrations in the PVP ring may be responsible for the absorption bands at 1110.8 cm^{-1}. Stretching vibration is responsible for the appearance of a peak at 1024 cm^{-1} indicatingC—O.[49] Similar results have been reported previously.[50] Figure 3(c) shows that after the addition of ZnO nanoparticles to SiO_2 nanoparticles, the absorption bands shifted to lower wavenumber for Si—O, Zn—O, C═O and C—H. The appearance of peaks that correspond to Si—O and Zn—O bonds is an indication of strong interaction between ZnO and SiO_2 nanoparticles. A similar result was reported by Chen *et al.*,[51] who immobilized ZnO on amorphous SiO_2 nanoparticles and observed a shift in the absorption band after the formation of ZnO/SiO_2 nanocomposites.

XRD analysis of ZnO, SiO_2 and ZnO/SiO_2

XRD was used to analyze the mineralogical phases of ZnO, SiO_2 and ZnO/SiO_2. The results are given in Fig. 4.

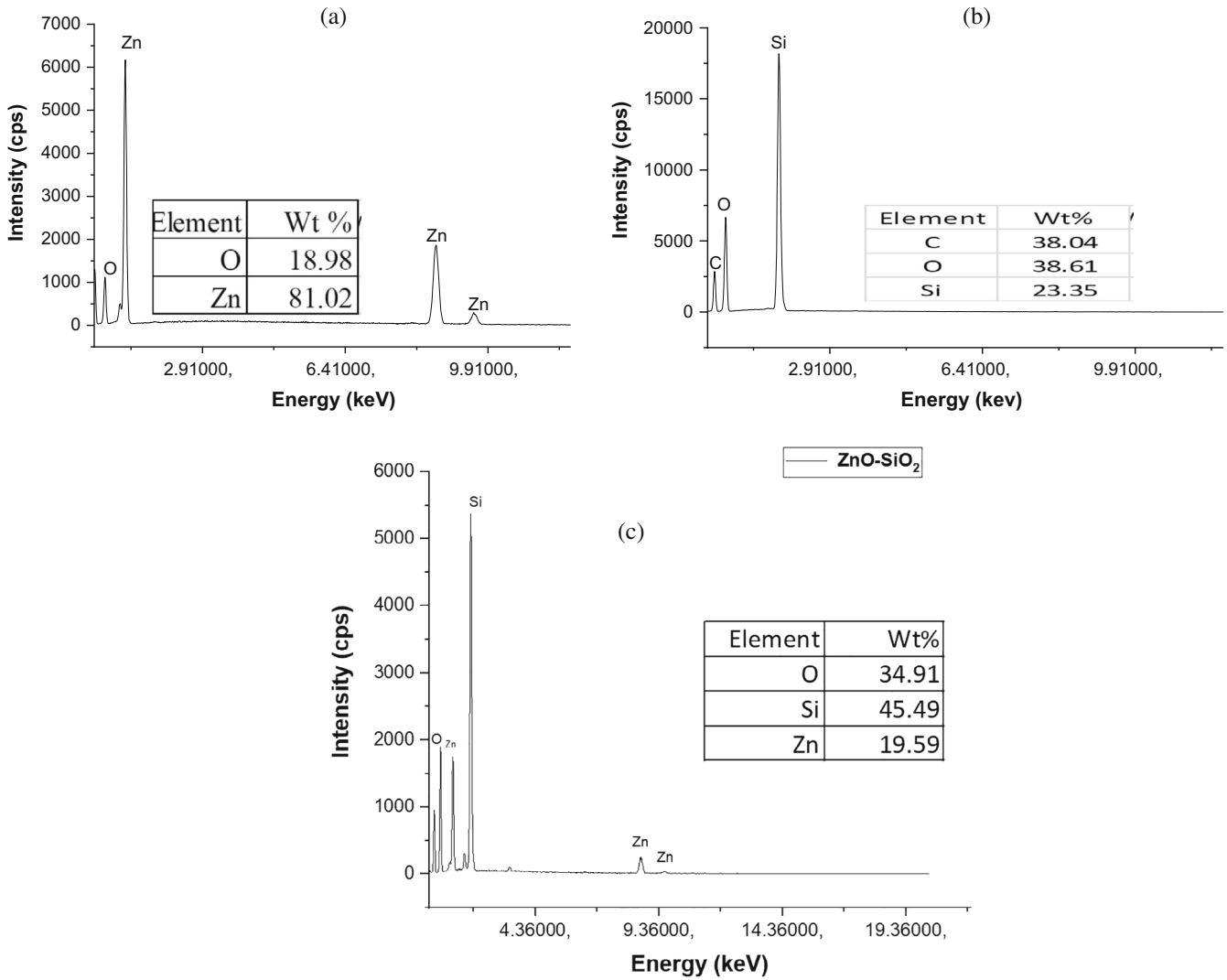

Figure 2. EDS traces of (a) ZnO, (b) SiO_2 and (c) SiO_2/ZnO nanorods.

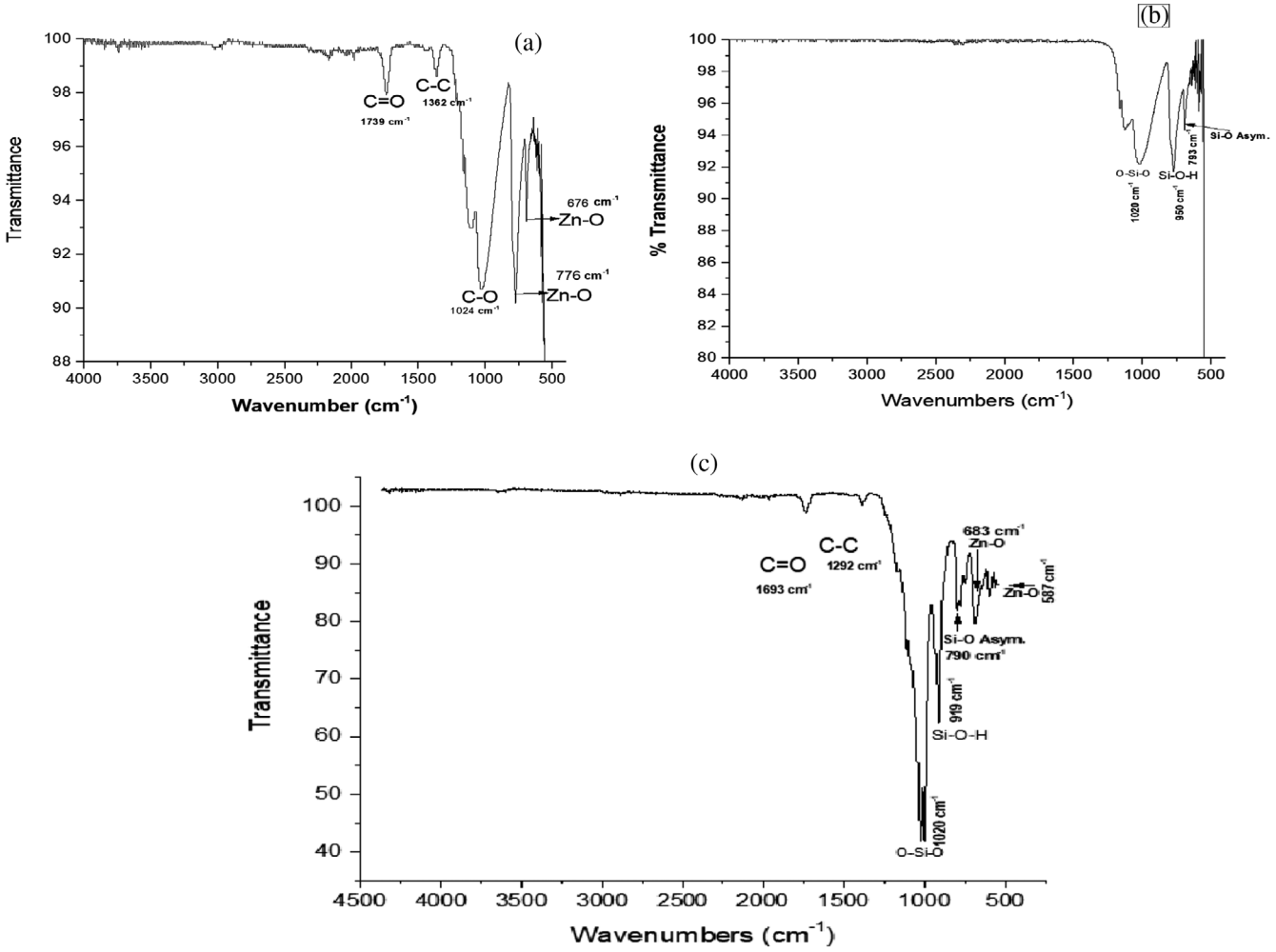

Figure 3. FTIR spectra of (a) SiO_2 nanoparticles, (b) ZnO nanoparticles and (c) ZnO/SiO_2 nanorods.

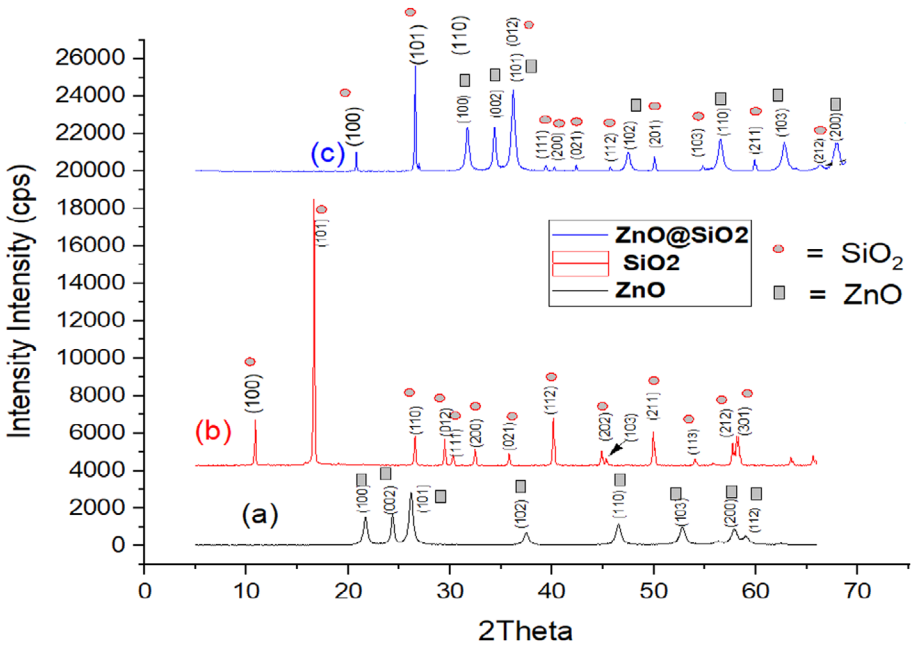

Figure 4. XRD patterns of (a) ZnO nanoparticles, (b) SiO_2 nanoparticles and (c) ZnO/SiO_2 composites.

Figure 4(a) indicates the presence of different peaks at 2θ values of 21.70°, 24.47°, 26.25°, 37.64°, 46.73°, 52.92°, 56.36, 58.02° and 59.12°, corresponding to hexagonal wurtzite zincite (ZnO) nanoparticles with crystal planes of (100), (002), (101), (102), (110), (103), (200) and (112). The diffraction peaks represent ZnO nanostructure with a hexagonal wurtzite phase where the oxygen atoms are arranged in a hexagonally close-packed structure with zinc atoms occupying half of the tetrahedral sites.[52] The peaks correspond to a lattice constant of $a = b = 3.242$ Å and $c = 5.205$ Å which match well with JCP2-36-1451. The ZnO nanoparticle crystallite size was determined to be 16.52 nm (see Eqn 13). These findings are in accordance with the report by Noukelag *et al.*[53] who synthesized ZnO nanoparticles via the green method using extract of *Rosmarinus officinalis* leaves. However, their analysis revealed that the ZnO nanoparticles had stronger diffraction and higher crystallinity than the ZnO nanoparticles prepared in the present study. This is not surprising due to the calcination temperature (500 °C for 2 h) used by those researchers during the synthesis of the ZnO nanoparticles. In contrast, in this study, the ZnO nanoparticles prepared were calcined at 450 °C for 2 h. Calcination temperature influences the crystallinity of a material.

Figure 4(b) indicates the presence of diffraction peaks at 2θ values of 10.81°, 16.51°, 26.49°, 29.39°, 30.22°, 32.39°, 35.71°, 40.04°, 44.77°, 45.21°, 49.86°, 53.90°, 67.62°, 68.19° and 73.29° which correspond to crystal planes of (100), (101), (110), (012), (111), (200), (021), (112), (202), (103), (211), (113), (212) and (301). This can be assigned to the hexagonal structure α-quartz phase of SiO_2 nanoparticles with a lattice constants $a = 4.92100$, $c = 5.41630$ Å and $Z = 3$ (JCP2-83-0539). The average crystallite of SiO_2 was 23.59 nm. The XRD pattern in Fig. 4(c) indicates the presence of ZnO with peaks at 2θ values of 31.63°, 34.45°, 36.24°, 47.64°, 56.56°, 62.81°, 67.67°, 68.05° and 69.34°, representing the Miller indices (100), (002), (101), (102), (110), (103), (200), (112) and (004), respectively. This corresponds to the hexagonal wurtzite phase (JCPDS 36-1541). The XRD pattern also shows intense and sharp diffraction peaks at 2θ values of 20.81°, 26.53°, 36.38°, 39.44°, 40.32°, 42.38°, 45.83°, 50.04°, 54.77°, 56.56°, 60.13°, 63.90°, 67.62° and 68.19° with corresponding crystal planes (100), (101), (110), (012), (111), (200), (021), (112), (202), (103), (211), (212) and (301), respectively. This matched well to crystalline SiO_2 nanoparticles with JCP2_83–0539 of the α-quartz phase of silica. Compared with the results for the pure ZnO and SiO_2 (Figs 4(a) and (b)), it is obvious that a composite of ZnO/SiO_2 was dominated by the quartz phase. After the formation of the ZnO/SiO_2 nanocomposite, the characteristic peaks of the pure SiO_2 nanoparticle with the ZnO nanoparticles did not change except that ZnO appears at a higher diffraction angle. Additionally, Fig. 4(c) indicates the formation of Zn_2SiO_4 which suggests the successful immobilization of SiO_2 nanoparticles onto the core–shell of ZnO nanoparticles due to the diffusion of silicon ions (Si^{4+}) with a small ionic radius of 0.26 Å into the core–shell of Zn^{2+} ions (0.74 Å). The crystallite size of the ZnO/SiO_2 rods was 15.36 nm. The result shows a decrease in crystallite size for the ZnO nanoparticles from 16.52 to 15.36 nm due to the addition of SiO_2 to the ZnO nanoparticle unit cell causing the cell to shrink, resulting in the formation of oxide clusters of Si–O–Zn. This is different from the result obtained by Rahmat *et al.*[54] Those authors reported high crystallinity of ZnO/SiO_2 nanocomposites and a higher shift of the diffraction angle (2θ) after the immobilization of ZnO and SiO_2 nanoparticles at a higher temperature. Other researcher reported a shift to a lower diffraction angle (2θ) after the immobilization of ZnO and SiO_2 nanoparticles.[55] This is an indication that immobilization of ZnO and SiO_2 at elevated temperatures could cause a change in the diffraction angle (2θ) with the same Miller indices. However, other researchers[56,57] have reported the synthesis of ZnO/SiO_2 nanocomposites without a shift to a lower or higher diffraction angle (2θ). The difference is that the authors did not subject the ZnO/SiO_2 nanocomposites produced to high-temperature treatment. The analysis by Bahrami and Karami[58] also confirmed that the addition of SiO_2 does not affect the ZnO crystal structure. However, the XRD result for SiO_2 nanoparticles and ZnO/SiO_2 nanocomposites reported by Chen *et al.*[51] shows an amorphous structure of both SiO_2 particles and ZnO/SiO_2 nanocomposites. This may be attributed to the fact that the authors did not subject the produced nanoparticles and the nanocomposites to temperature treatment.[59]

The crystallite size was calculated using the following equation:

$$D = \frac{k\lambda}{\beta\cos\theta} \tag{13}$$

where k is the particle shape correction factor (0.9), D is the crystallite size, θ is the Bragg angle and λ is the wavelength of the Cu target.

XPS analysis of SiO_2 nanoparticles

General XPS analysis of the SiO_2 nanoparticle was conducted to determine the chemical oxidation states of elements. The XPS general survey and deconvoluted spectra of O (1s) and Si (2p) of the SiO_2 nanoparticles are presented in Fig. 5.

The full XPS scan spectrum of SiO_2 nanoparticles is shown in Fig. 5(a). With electron core-level XPS spectra of O (1s), O (2s), Si (2p), Si (2s) and C (1s), the result confirms the existence of silicon, oxygen and carbon components in the sample. For the Si (2s) signal peak, the result confirms the presence of Si species at 154.2 eV. The presence of a carbon atom with a binding energy of 286 eV could be owing to the quartz sand's inherent carbon. Figure 5(b) shows the presence of a peak at a binding energy of 106.72 eV indicating the presence of pure SiO_2 with Si^{4+}. In Fig. 5(c) the O 1s signal peak appears at a binding energy of 536.3 eV and suggests the presence of oxygen in the SiO_2 nanoparticles. The result obtained from this study is different from the 532.3 eV reported by Zenkovets *et al.*[60] due to the differences in the method, precursors and other processes used during the synthesis of SiO_2 nanoparticles.

XPS analysis of ZnO nanoparticles

Figure 6 shows the XPS spectra of ZnO nanoparticles. Figure 6(a) shows different peaks at 1021.80 and 1045.07 eV which were related to Zn ($2p_{3/2}$) and Zn ($2p_{1/2}$) core levels. The two peaks have narrow linewidths suggesting the dominance of the Zn^{2+} ions in the nanoparticles.[61] The binding energy difference between $2p_{3/2}$ and $2p_{1/2}$ peaks is 23.27 eV, indicating that the Zn (2p) peak has significantly split spin–orbit components. This is within the standard value of 23.0 eV for Zn^{2+}.[62] A similar value (23.00 eV) has been reported previously[63] for ZnO nanoparticles, though obtained with different synthetic methods. This result confirms that the Zn exists mostly as Zn^{2+} surrounded by the O^{2-} oxidation state in the hexagonal wurtzite ZnO form. The spectrum also shows a peak at 284.60 eV corresponding to C (1s) which indicates a considerable concentration of organic molecules adsorbed onto the surface of the nanoparticles from the PVP used as a structure-directive agent during the synthesis of the ZnO nanoparticles. Figure 6(b), which represents the high-

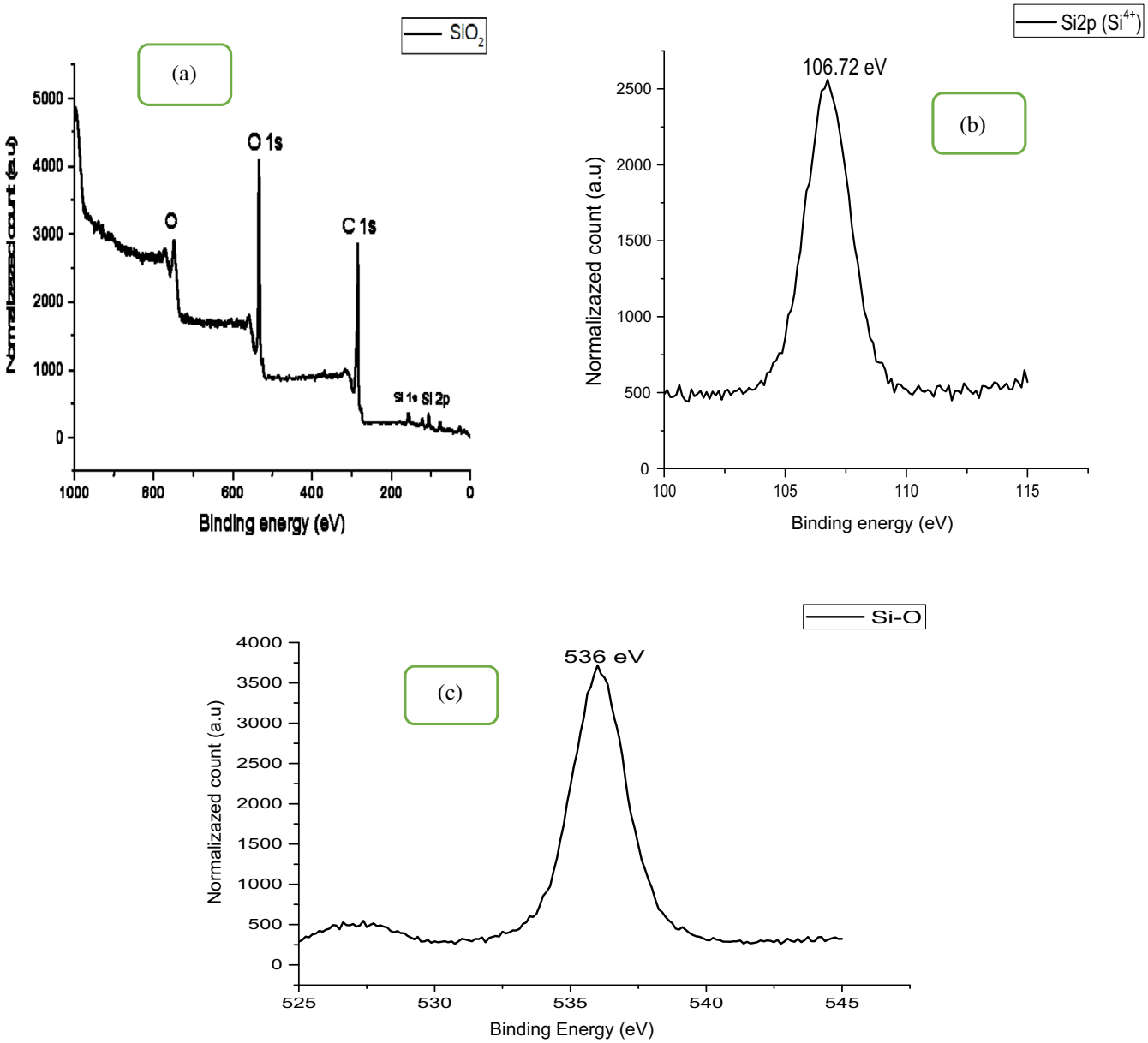

Figure 5. (a) XPS general survey spectrum and XPS spectra of (b) O 1s and (c) Si 2p of SiO_2 nanoparticles.

resolution XPS result for Zn $2p_{3/2}$ (ZnO), shows the appearance of a single broad peak at a binding energy of 1021.80 eV. This further indicates the presence of a highly electropositive zinc ion (Zn^{2+}) with two donated electrons in a strongly electronegative environment with charged O^{2-} ions. The Zn $2p_{3/2}$ peak, with a binding energy of 1021.80 eV, was only fitted to one Gaussian with a geometry of a hexagonal wurtzite structure. This result agrees with previous findings,[64,65] reporting the presence of ZnO at 1022.6 and 1022.15 eV. The differences observed in the binding energies reported in this work compared to those of previous studies are not surprising based on the report by Gao *et al.*[66] that the Auger parameter of metal at the nanoscale changes the binding energy of Zn photoelectrons.

Figure 6(c) shows three different peaks at binding energies of 530.6, 532.2 and 533.5 eV. The peak located at 530.6 eV is characteristic of ZnO (bond between Zn and O) usually called the zinc oxide peak. The result from this analysis agrees with the conclusion of Bourlier *et al.*[67] that the O (1s) atom with a binding energy between 527 and 530 eV is typical of O^{2-} ions in metal oxides. While binding energies between 530.6 and 531.1 eV are typical of the species of oxygen incorporated in the form of ZnO. The binding energies between 531.1 and 532 eV may be due to low coordinated oxygen species described as O^{-} ions capable of forming compounds such as C═O and COO^{-}.[68] Peaks in the XPS spectrum for O (1s) at binding energy equal to 530 or 532 eV corresponding to ZnO and binding energy around 530.6, 532.2 and 533.2 eV were ascribed to O^{2-}, O^{-} and ions respectively.[69] Additionally, the binding energies at 530.6 and 532.2 eV for O^{2-} and O^{-} respectively were assigned to O–Zn–O and $Zn(OH)_2$ respectively.[70]

XPS analysis of ZnO/SiO_2 nanorods

Chemical states of different elements within the core–shell of ternary ZnO/SiO_2 nanorods were determined using XPS. The results are displayed in Fig. 7.

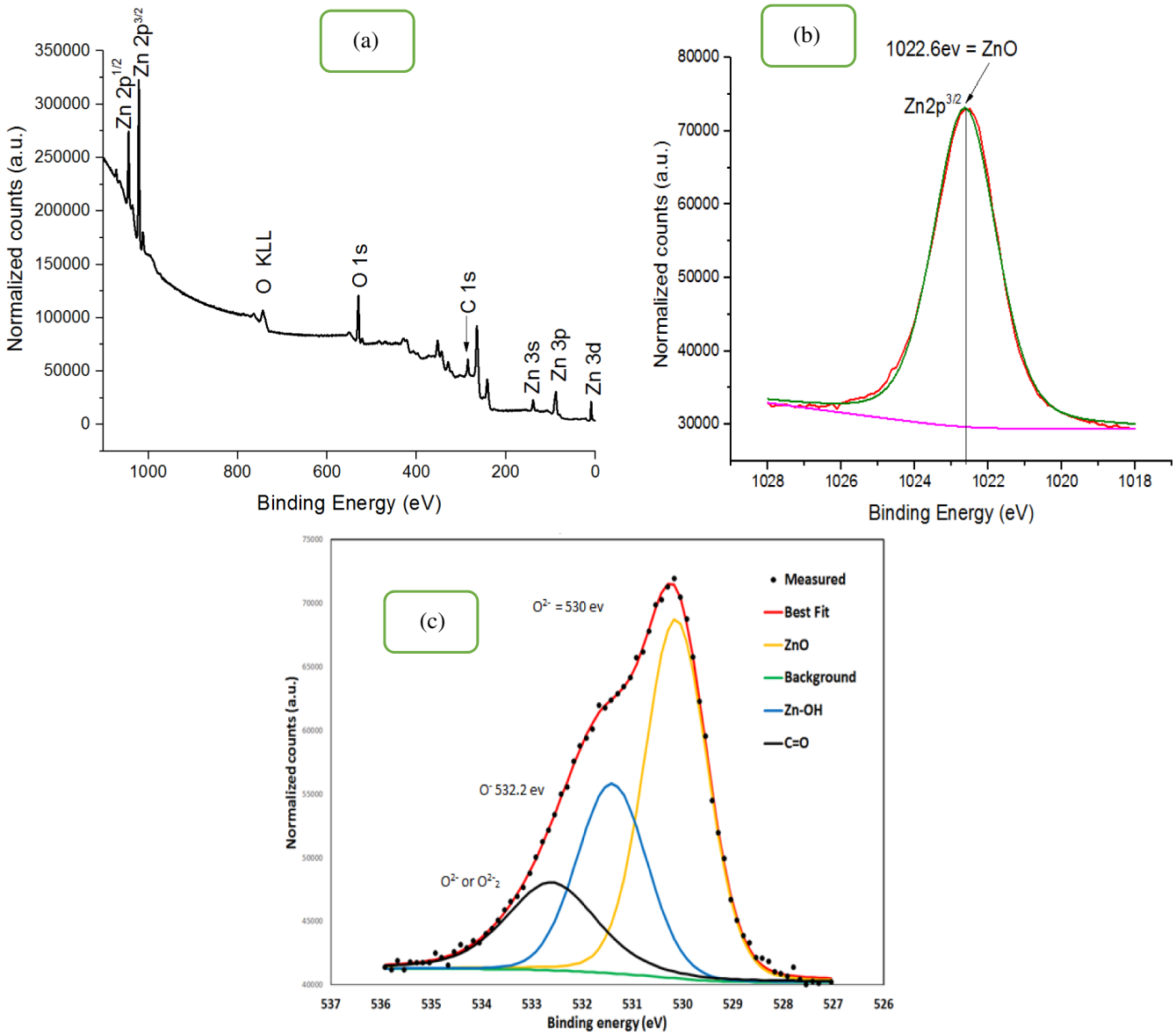

Figure 6. (a) XPS general survey spectrum and XPS spectra of (b) Zn $2p_{3/2}$ and (c) O (1s) core level of ZnO nanoparticles.

Figure 7(a) shows the presence of peaks at a binding energy of 103.78 eV confirming the existence of Si in SiO_2 nanoparticles. The peaks at 1047 and 1025.1 eV represent Zn $2p_{1/2}$ and Zn $2p_{3/2}$, respectively, suggesting that the zinc occurs in the form of a Zn^{2+} chemical state on the sample surfaces. The C (1s) peak at 285.6 eV indicates the presence of adventitious carbon atoms originating from the PVP used as a structure-directing agent for the synthesis of pure ZnO.

The appearance of a peak at binding energy of 531.16 eV in Fig. 7(b) shows that only Si–O–Si or SiO_2-like bonds were present in the composites. This result is different from that of other researchers reporting peaks corresponding to Si—Si, Si—OH and C—O bonds.[70] The differences observed in this work compared with previous research may be due to the methods, conditions applied and chemical precursors used for the synthesis of the nanorods. Additionally, the result confirmed the stability of SiO_2 after the formation of the ZnO/SiO_2 nanorods. Figure 7(c) shows the Zn (2p) spectrum with peaks at 1045.63 and 1022.63 eV associated with Zn ($2p_{1/2}$) and Zn ($2p_{3/2}$), suggesting Zn element in the ZnO/SiO_2 nanorods present only in one valence state (Zn^{+}) as against the Zn^{2+} reported earlier for the pure ZnO nanorods. The presence of Zn with only one valence state indicates the formation of bonds with Si and O. The XPS patterns of the Zn (2p) for ZnO/SiO_2 nanorods show two peaks compared to only one peak for Zn (2p) in ZnO nanoparticles. This suggests the existence of Zn (+1) oxidation in ZnO/SiO_2 nanorods compared to (+2) valence state in pure ZnO nanoparticles. The oxidation of the state of Si in ZnO/SiO_2 nanorods remained (+4) after the formation of ZnO/SiO_2 nanorods.

BET analysis of ZnO and SiO_2 nanoparticles and ZnO/SiO_2 nanorods

BET measurements were used to study the surface area of ZnO and SiO_2 nanoparticles and ZnO/SiO_2 nanorods. The result is presented in Fig. 8.

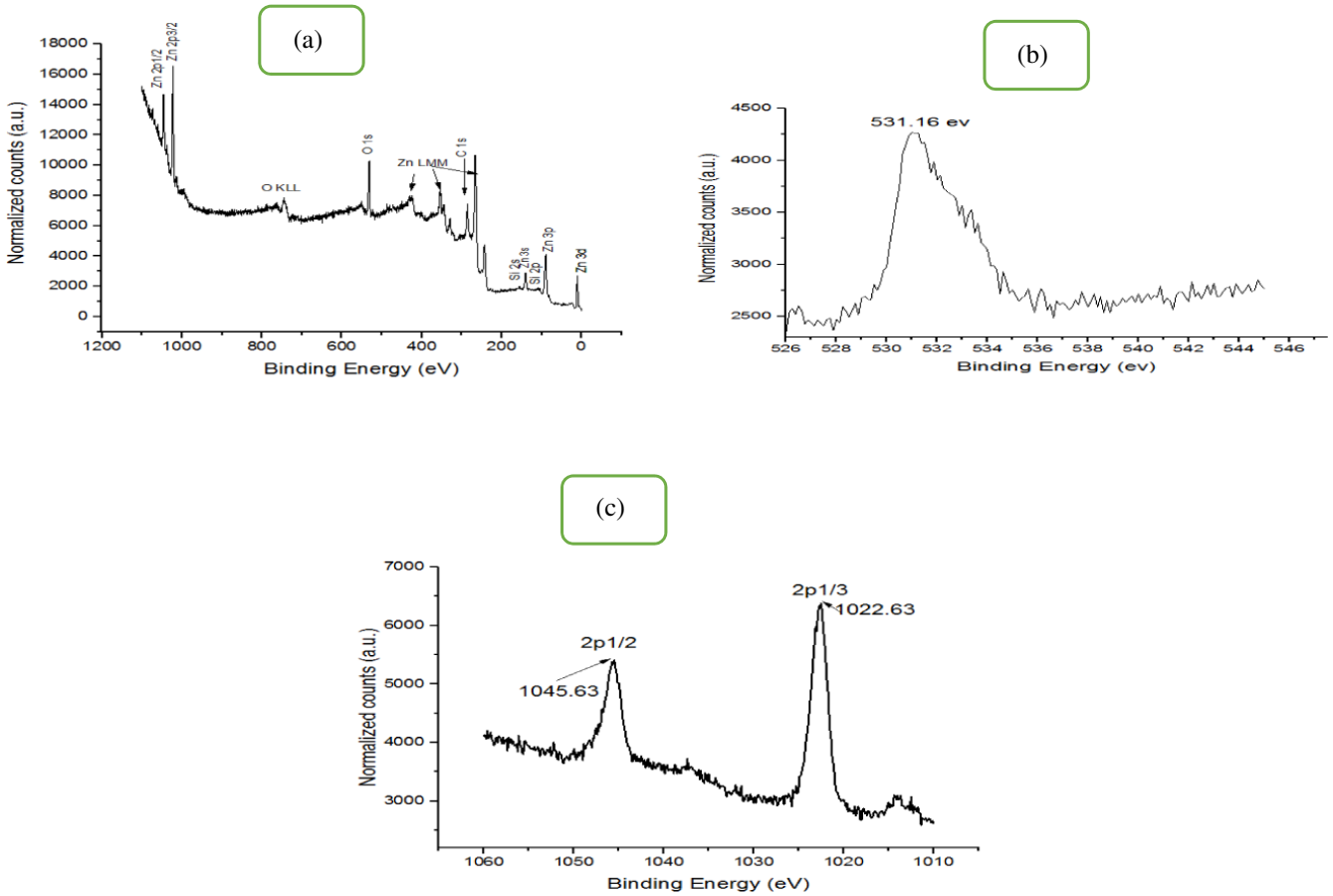

Figure 7. XPS general survey of (a) ZnO/SiO_2 nanorods and XPS core level of (b) SiO_2 and (c) ZnO nanoparticles.

According to the IUPAC classification, adsorption isotherms are classified into Type I, Type II, Type III and Type IV. Based on the curves in Fig. 8, it can be noticed that all three samples exhibited a Type IV isotherm characteristic of mesoporous materials. Figure 8(a) shows that the hysteresis loops were formed at a relative pressure of 0.57–0.98. A relative pressure of 0.7–1.5 was recorded for ZnO in Fig. 8(b). Hysteresis loops in the relative pressure range 0.8–0.98 were recorded for ZnO/SiO_2 nanorods. The results show that the volume of nitrogen adsorption increases with relative pressure until a limit is reached, indicating the availability of pores.

It is evident from Table 2 that ZnO/SiO_2 nanorods had the highest surface area (33 $m^2\ g^{-1}$) compared with the 0.386 and 8.620 $m^2\ g^{-1}$ recorded for the SiO_2 and ZnO nanoparticles. The enhancement in the surface area can be linked to the change of the nanoparticles from spherical to rod-like structures, which results in the creation of more active sites due to more atoms on the surface and edges of the composite. This result suggests that the ZnO/SiO_2 nanorods may have a higher adsorption capacity compared to the ZnO and SiO_2 nanoparticles. Materials with a high surface area are advantageous for adsorption because such a surface area provides more active sites for adsorption.[71] Table 2 also indicates that SiO_2 and ZnO nanoparticles and the ZnO/SiO_2 nanorods had pore volumes of 0.002, 0.353 and 0.166 $cm^3\ g^{-1}$, respectively. The inset plots in Figs 8(a)–(c) indicate that the pore diameters for SiO_2 and ZnO nanoparticles and the ZnO/SiO_2 nanocomposites were 32.150, 13.173 and 26.946 nm, respectively. According to the IUPAC classification of pore sizes, materials with pore widths between 2 and 50 nm are categorized as mesoporous materials.[72]

Physicochemical properties of refinery wastewater

The physicochemical properties of the refinery wastewater were examined. The result is presented in Table 3.

Table 3 presents the physicochemical parameters such as pH, temperature, conductivity, COD, BOD and content of lead and cadmium. The pH value obtained was 6.25, which is lower than the 6.51–8.5 recommended by the WHO. The low pH could have been caused by dissolved organic carbon in the wastewater.[73] The temperature recorded in Table 3 indicates that the temperature value was closer to the recommended values of the WHO. This observation could be because water has a large specific heat capacity, which implies it takes more energy to raise its temperature than other substances. The high temperature may reduce the amount of dissolved air in water, which could lead to aquatic organism mortality.[74] Electrical conductivity decreases, indicating that the sample contains a significant number of dissolved ions, forming a barrier to organism survival. The refinery wastewater has high values of COD and BOD compared to the 40 and 1 mg L^{-1} recommended by the WHO.[75] This is an indication that the sample contained a very high concentration of organic pollutants. Additionally, the higher the BOD, the faster the oxygen in the wastewater is lost, indicating that

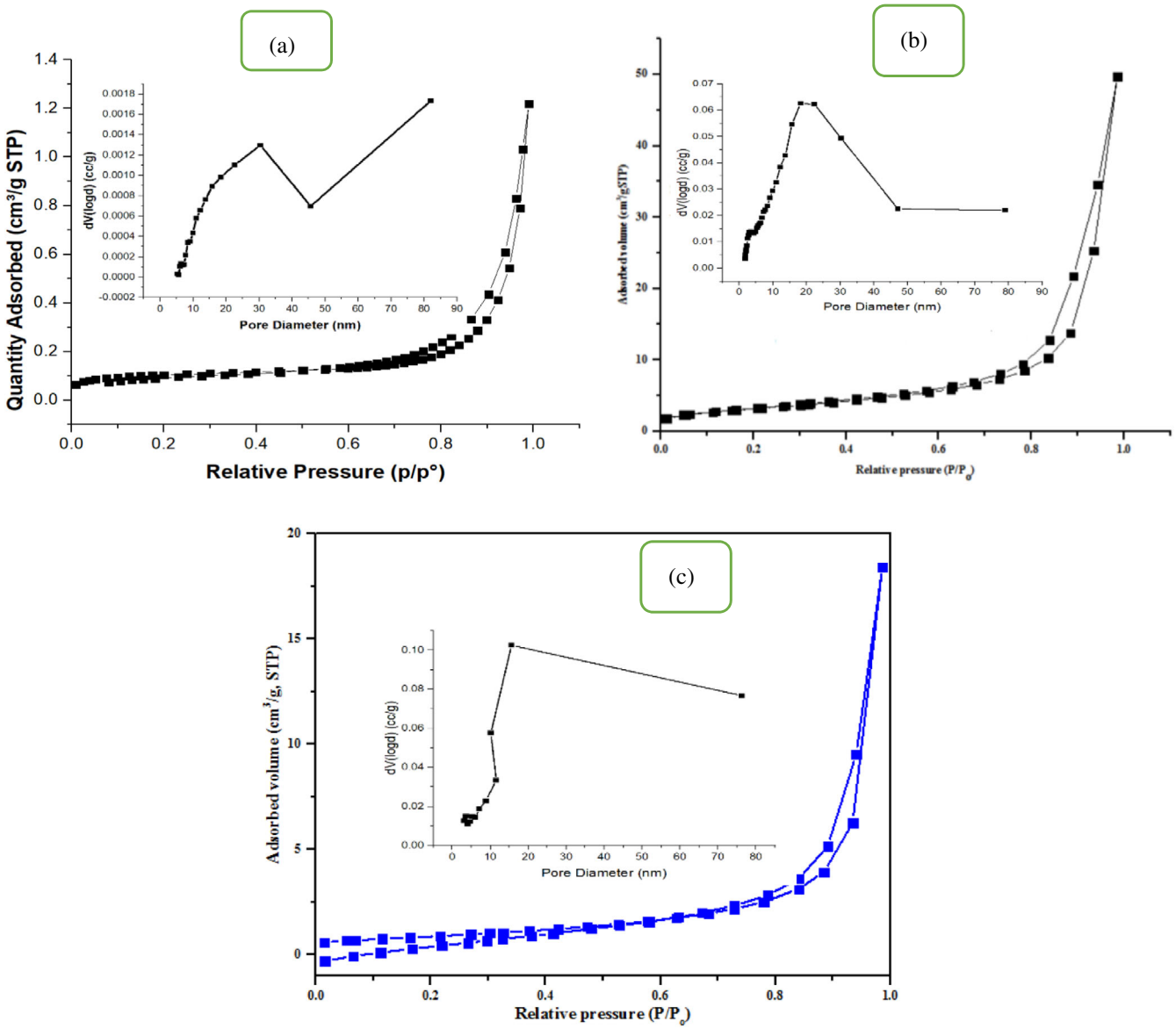

Figure 8. BET pore size and pore diameter distributions for (a) SiO_2 nanoparticles, (b) ZnO nanoparticles and (c) ZnO/SiO_2 nanorods.

Table 2. Surface area, total pore volume and pore diameter of ZnO and SiO_2 nanoparticles and ZnO/SiO_2 nanorods

Sample	BET surface area ($m^2\ g^{-1}$)	Total pore volume ($cm^3\ g^{-1}$)	BJH pore diameter (nm)
SiO	0.386	0.002	32.150
ZnO	8.620	0.353	26.173
ZnO/SiO_2	33.469	0.166	15.946

less oxygen is available to aquatic life leading to stress, suffocation and death of aquatic organisms.[76] Table 3 also presents the concentration of lead and cadmium with lead having the highest concentrations. The concentration of the two heavy metals was greater than the recommended limits of the WHO. Because both Pb(II)and Cd(II) ions are extremely harmful even at small concentrations, removing them from the refinery wastewater before their discharge into the environment is critical. Other physicochemical parameters of the refinery wastewater before and after batch adsorption are presented in Table S1 (supporting information).

Batch adsorption studies

Effect of contact time

The contact time has an important effect on the process of adsorption.[77] This is the most essential component that governs the adsorption process efficiency and also impacts the adsorption process economic efficiency. The elimination of Pb(II) and Cd(II) from refinery wastewater using ZnO and SiO_2 nanoparticles and ZnO/SiO_2 nanorods was investigated at various time intervals (1–25 min). The results are given in Fig. 9.

Figures 9(a) and (b) show the adsorption of Pd(II) and Cd(II) ions, respectively, from the refinery wastewater between 0 and 25 min. It was found that the removal of both Pd(II) and Cd(II) was slow between 0 and 5 min and rapidly increases during min, after

Table 3. Physicochemical parameters of refinery wastewater before and after batch adsorption

Parameter	Value before adsorption	Value after adsorption			WHO permitted limit (2017)[a]
		ZnO/SiO_2	ZnO	SiO_2	
Chemical oxygen demand (COD), mg L^{-1}	880.15 ± 0.30	52.05 ± 0.20	60 0.20 ± 0.10	73.75 ± 0.12	40
Biological oxygen demand (BOD), mg L^{-1}	190.32 ± 0.20	37.41 ± 0.10	58.01 ± 0.0.03	62.34 ± 0.05	1
Total organic carbon (TOC), mg L^{-1}	560.12 ± 0.03	84. 90 ± 0.05	93.02 ± 0.1	97.64 ± 0.08	—
Lead (Pb), mg L^{-1}	1.94 ± 0.06	0.26 ± 0.10	0.56 ± 0.06	0.52 ± 0.10	0.003 ± 0.04
Cadmium (Cd), mg L^{-1}	1.28 ± 0.10	0.244 ± 0.03	0.37 ± 0.02	0.39 ± 0.05	0.05 ± 0.10
Temperature (°C)	31.20 ± 0.12	30.12 ± 0.15	31.34 ± 020	31.45 ± 0.15	30
pH	6.25 ± 0.10	7.16 ± 0.01	6.60 ± 0.12	6.75 ± 0.10	6.51–8.5
Electrical conductivity (μS cm^{-1})	483.74 ± 0.13	72.53 ± 0.14	98.83 ± 0.10	91.06 ± 0.12	—

[a] WHO, World Health Organization.

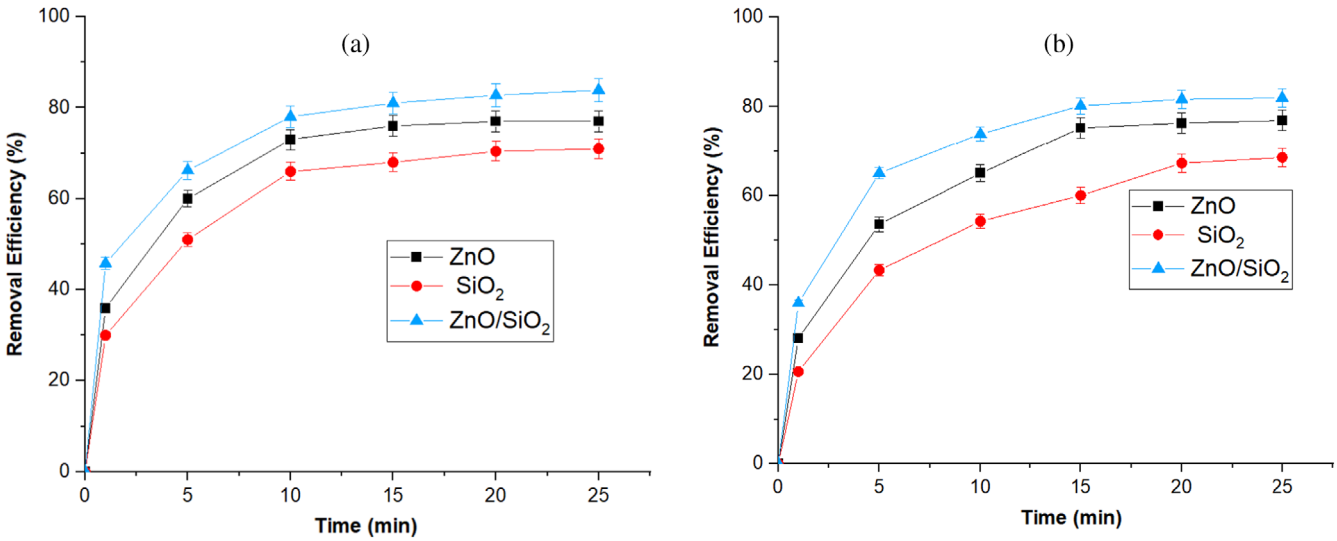

Figure 9. Influence of contact time on removal of (a) Pb(II) and (b) Cd(II) at pH 6.25, 30 °C and adsorbent dose of 0.05 g.

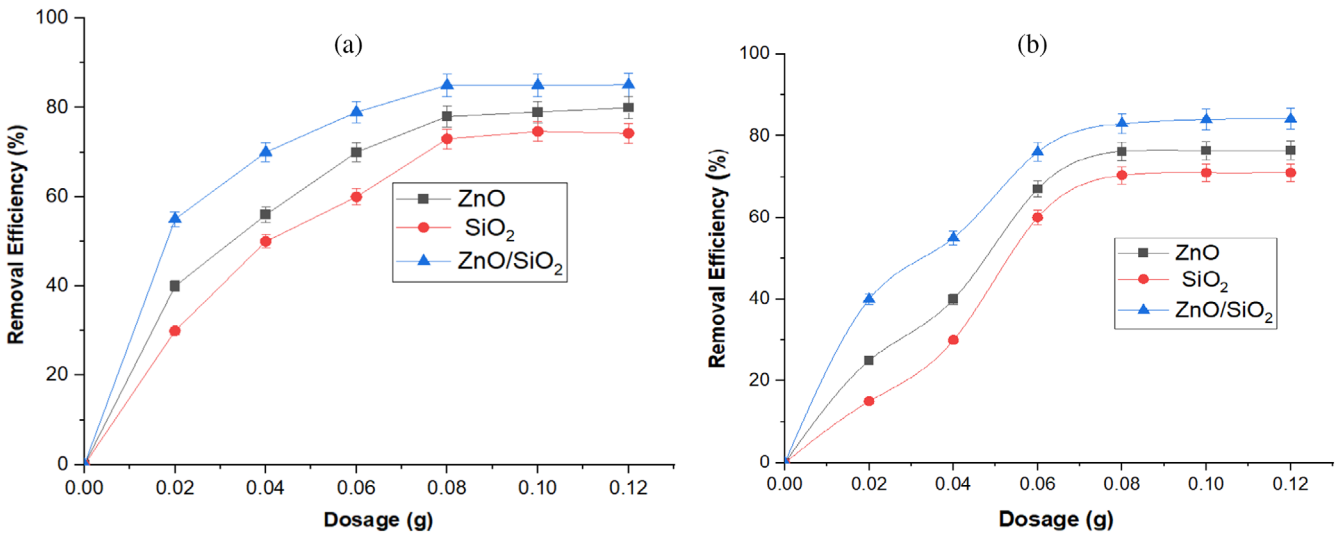

Figure 10. Influence of nanoadsorbent dosage on adsorption of (a) Pb(II) and (b) Cd(II) at 30 °C and contact time of 15 min.

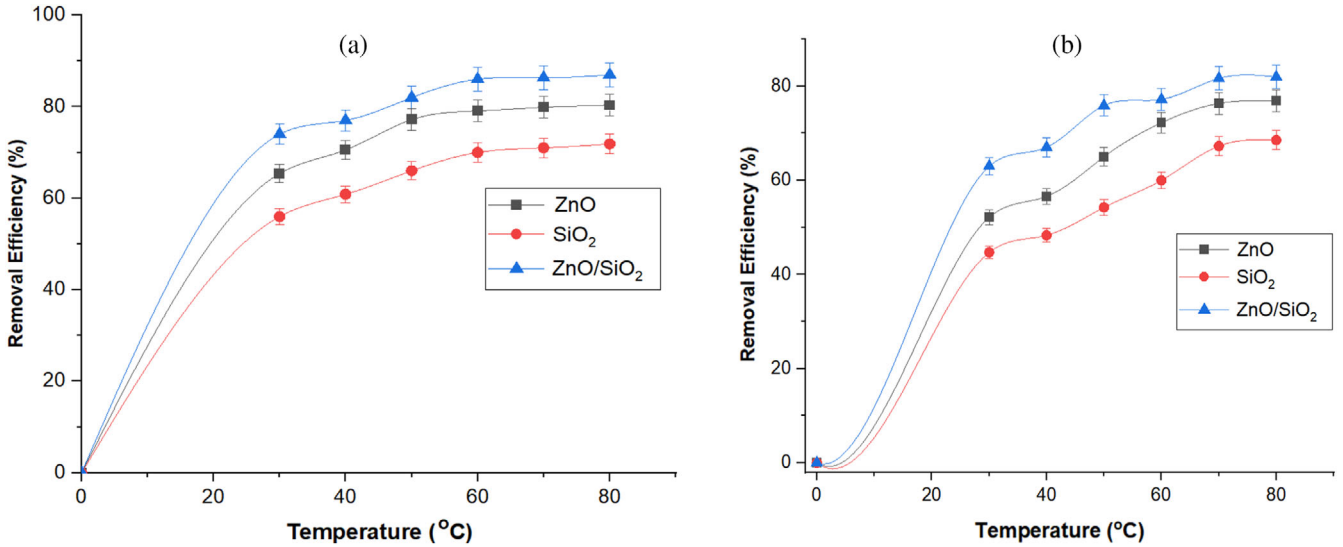

Figure 11. Influence of reaction temperature on removal of (a) Pb(II) and (b) Cd(II) for contact time of 15 min and adsorbent dosage of 0.05 g.

Table 4. Adsorption isotherm models for removal of Pb(II) and Cd(II) ions from petrochemical refinery wastewater by selected nanoadsorbents

		Pb(II)			Cd(II)		
Model	Parameters	ZnO	SiO_2	ZnO/SiO_2	ZnO	SiO_2	ZnO/SiO_2
Langmuir	q_{max} (mg g^{-1})	30.772	24.860	37.951	30.328	20.124	33.603
	K_L	5.369	4.768	5.764	0.133	0.090	0.526
	R_L	0.026	0.029	0.024	0.785	0.844	0.48
	R^2	0.998	0.996	0.998	0.992	0.988	0.993
	SSE	0.058	0.053	0.070	0.049	0.054	0.081
	x^2	0.326	0.417	0.035	0.530	0.859	0.067
Freundlich	K_F (mg g^{-1})	0.079	0.060	0.161	0.719	0.587	0.341
	$1/n$	0.077	0.084	0.067	0.082	0.084	0.083
	R^2	0.952	0.939	0.959	0.989	0.978	0.975
	SSE	0.135	0.137	0.135	0.138	0.143	0.140
	x^2	0.267	0.269	0.252	0.270	0.365	0.292
Temkin	K_T (L mg^{-1})	1.658	1.848	1.224	2.007	2.235	1.458
	B (J mol^{-1})	306.790	262.271	625.113	222.299	196.548	364.649
	R^2	0.995	0.868	0.898	0.890	0.884	0.894
	SSE	3.1572	3.542	2.283	39.763	45.671	27.772
	x^2	3.854	4.315	2.751	48.545	55.637	33.467
D-R	q_{max} (mg g^{-1})	11.115	11.132	14.801	10.433	10.251	12.449
	B_D (mol kJ^{-2})	2.06×10^{-7}	2.05×10^{-7}	2×10^{-7}	4×10^{-7}	4.02×10^{-7}	3.90×10^{-7}
	E (kJ mol^{-1})	1556.496	1560.087	1581.139	1461.139	1581.139	1785.16
	R^2	0.846	0.835	0.861	0.826	0.822	0.850
	SSE	0.158	0.154	0.163	1.8732	1.305	0.976
	x^2	1.984	1.983	1.985	4.592	6.827	2.318

which the removal efficiency further increased, however at a much slower rate, until it reaches equilibrium after 15 min of interaction with the nanoadsorbents. The rapid adsorption rate at the start (10 min) was attributable to the higher number of surface adsorption sites, after which the adsorption achieved a steady state.[78] This may also be ascribed to significant interaction between the nanoadsorbent and the adsorbate, leading to greater removal of the heavy metals. As the contact time increases, the heavy metals occupy the active sites leading to their blockage.[79] Accordingly, the adsorption pattern was in the order Pb(II) (77.00%, 70.99% and 83.88%) > Cd(II) (76.91%, 68.54% and 81.98%) for SiO_2, ZnO and ZnO/SiO_2 nanorods, respectively. The trend observed shows that the ionic radius of the heavy metal ions plays a critical role in the removal of the heavy metal. The ionic radius is in the order Pd(II) (1.19 Å) > Cd(II) (0.97 Å). The greater the ionic radius of a metal ion, the greater its removal due to the lower hydration potential of the heavy metal ion. A similar pattern has been observed previously,[80,81] the authors reporting higher removal of 98.0% for Pb(II) and 97.3% for Cd(II). A similar trend has been observed by Rodríguez *et al.*,[82] who

Table 5. Kinetic models for adsorption of Pb(II) and Cd(II) from petrochemical refinery wastewater using various nanoadsorbents

Selected heavy metal	Nanomaterial	Pseudo-first order					Pseudo-second order					Intraparticle diffusion			Elovich		
		R^2	k_1 (mg g^{-1} min^{-1})	q_{e1} (g min^{-1})	SSE	χ^2	R^2	k_2 (mg g^{-1} min^{-1})	q_{e2} (g min^{-1})	SSE	χ^2	R^2	k_{id} (g min^{-1})	C	R^2	β	α (g m^{-1})
Pb(II)	ZnO	0.863	0.159	0.087	0.415	4.712	0.990	4.413	0.269	0.016	0.203	0.822	0.031	0.020	0.900	58.309	0.086
	SiO_2	0.753	0.149	0.086	0.457	5.753	0.983	2.936	0.244	0.023	0.294	0.793	0.012	0.012	0.890	51.600	0.083
	ZnO/SiO_2	0.881	0.175	0.092	0.364	4.487	0.993	5.425	0.272	0.012	0.129	0.841	0.012	0.031	0.926	60.643	0.181
Cd(II)	ZnO	0.954	0.158	0.103	0.456	6.059	0.987	2.468	0.278	0.029	0.407	0.861	0.013	0.005	0.932	53.908	0.080
	SiO_2	0.921	0.154	0.087	0.486	6.819	0.953	1.271	0.286	0.085	0.736	0.843	0.010	0.001	0.897	45.704	0.034
	ZnO/SiO_2	0.954	0.162	0.094	0.399	4.758	0.996	4.427	0.314	0.017	0.169	0.877	0.016	0.019	0.944	56.465	0.134

studied the potential of graphene oxide–ZnO nanoadsorbent for the removal of heavy metal ions. In their analysis, they reported the rapid removal of the heavy metals between 30 and 60 min. The high percentage adsorption of Cd(II) and Pd(II) by the ZnO/-SiO_2 nanorods could be related to the formation of new material (Zn_2SiO_4), enhanced surface area (Fig. 1(c) and Table 2) and the crystallite size of the nanocomposites compared with the individual nanoparticles. Additionally, the high adsorptive potential of ZnO nanoparticles compared to SiO_2 nanoparticles may be linked to the presence of more functional groups in the former than in the latter.

Effect of adsorbent dose

The adsorbent dose is one of the most critical factors impacting the performance of adsorbents in the removal of pollutants from wastewater.[83] Adsorbent dosage controls the availability of the binding sites during adsorption.[84] Thus, the adsorbent dosage was investigated to assess the adsorptive potential of ZnO and SiO_2 nanoparticles and ZnO/SiO_2 nanorods for the elimination of Pb(II)and Cd(II) from refinery wastewater. The results are given in Fig. 10.

Amounts of 0.02, 0.04, 0.06, 0.08, 0.1 and 0.12 g per 50 cm^3 of adsorbent were used. It was observed that increasing the nanoadsorbent dosage from 0.02 to 0.12 g per 50 cm^3 results in an increase in the removal of Pb(II) and Cd(II) to 1.0 g per 50 cm^3, after which the percentage adsorption removal remains constant. This observation may be linked to more active sites on the nanoadsorbent surface as the dosage increases.[85] Figure 10(a) shows Pd(II) has maximum removal efficiency of 80.00%, 74.25% and 85.06% while Cd(II) shows removal efficiency of 76.48%, 70.99% and 84.12% for ZnO and SiO_2 nanoparticles and ZnO/SiO_2 nanorods, respectively. The high adsorption of the ZnO/SiO_2 nanorods may be linked to their high surface area and crystallite size compared with the individual nanoparticles (ZnO and SiO_2).

Effect of adsorption temperature

One of the most critical parameters in adsorption processes is temperature.[86] The effect of various temperatures on the removal of Pd(II) and Cd(II) from refinery wastewater was examined. The results are presented in Fig. 11.

It was observed that for all of the nanoasorbents employed, the removal efficiency increases as the reaction temperature rises, suggesting that the elimination process of Pb(II) and Cd(II) is an endothermic reaction. This observation is different from the adsorption principle, which states that adsorption decreases as temperature rises and the adsorbate that is adsorbed on a surface is desorbed at a higher temperature.[87] This difference may be linked to an increase in the molecular kinetic or thermal energy, making Pb(II) and Cd(II) more mobile and increasing molecular motion, which allowed the adsorbate to enter pores more easily, as well as increased binding site activity, as the temperature rises.[88] This increase in metal ion removal efficiency could be attributable to the adsorption sites created by the breaking or rupture of some internal bonds along with the nanoparticle and nanorod edges at high temperatures.[89] Additionally, the direct relationship between the reaction temperature and the removal efficiency may be ascribed to the increase in the solubility of the metal ions as the reaction temperature increases.[90] The increase in removal efficiency as the temperature increases is evidence that temperature has a significant impact on the elimination of Pb(II) and Cd(II) ions, which suggests that the adsorption process involved chemical reaction (chemisorption) as reported

Table 6. Thermodynamic characteristics for adsorption of Pd(II) and Cd(II) from refinery wastewater

Selected heavy metal	Nanomaterial	ΔH (kJ mol^{-1})	ΔS (J mol^{-1} K^{-1})	ΔG (kJ mol^{-1})					
				303 K	313 K	323 K	333 K	343 K	353 K
Pb(II)	ZnO	17.595	31.811	6.071	5.767	5.462	5.158	4.854	4.550
	SiO_2	22.747	48.805	7.959	7.471	6.983	6.495	6.007	5.519
	ZnO/SiO_2	21.842	55.560	5.008	4.452	3.897	3.341	2.769	2.129
Cd(II)	ZnO	16.134	32.351	6.332	6.008	5.685	5.361	5.038	4.714
	SiO_2	9.661	10.759	7.956	7.638	7.320	7.002	6.684	6.366
	ZnO/SiO_2	26.184	66.147	6.141	5.480	4.818	4.157	3.495	2.834

previously.[91] Another observation from the analysis is that the ZnO/SiO_2 nanorods exhibited higher adsorption compared with the individual ZnO and SiO_2 nanoparticles, due to there being more adsorption sites in the former compared with the latter. ZnO/SiO_2 nanorods have more functional groups on their surface, making them a potential adsorbent for metal ion complexation via both electrostatic and coordination processes.[92]

Adsorption isotherms

The results of the batch adsorption of Pb(II) and Cd(II) from refinery wastewater were examined using the Freundlich, Langmuir, Temkin and D-R isotherms, as presented in Table 4.

Table 4 presents the results of the various isotherm models for the removal of Pb(II) and Cd(II). The findings indicate that the adsorption of Pb(II) fits better the Langmuir isotherm model with correlation coefficient (R^2) values of 0.998, 0.996 and 0.998 for ZnO and SiO_2 nanoparticles and ZnO/SiO_2 nanorods, while the adsorption process of Cd(II) ions with ZnO, SiO_2 and ZnO/SiO_2 exhibited R^2 values of 0.992, 0.988 and 0.993, respectively. The x^2 and the sum of square error (SSE) statistics were also used to evaluate the goodness fit of the isotherm for the removal of Pb(II) and Cd(II) using ZnO and SiO_2 nanoparticles and ZnO/SiO_2 nanorods from refinery wastewater. It is evident from Table 4 that the Langmuir isotherm model has the lowest error function values, which suggests the removal of Pb(II) and Cd(II) using ZnO and SiO_2 nanoparticles and ZnO/SiO_2 nanorods from refinery wastewater best fits the Langmuir isotherm model. This suggests that adsorption mechanisms involve monolayer adsorption. The order of the fits to the models were Langmuir > Freundlich > Temkin > D-R. The maximum adsorption capacity (q_{max}) values for metal ion binding to ZnO and SiO_2 nanoparticles and ZnO/SiO_2 nanocomposites followed the sequence 37.951 > 30.772 23.860 > 24.860 mg g^{-1} for Pb(II) and 33.603 > 30.328 > 20.124 mg g^{-1} for Cd(II), respectively. The dimensionless R_L value from Table 4 ranges from 0.231 to 0.844, which is smaller than 1, indicating that the adsorption process is favorable for ZnO and SiO_2 nanoparticles and ZnO/SiO_2 nanorods. The K_L value is a criterion for determining the affinity of absorbent and adsorbate molecules. The values obtained for Pb(II) were 5.369, 4.768 and 5.764 while those for Cd(II) were 0.133, 0.090 and 0.526 for ZnO/SiO_2 nanocomposites and ZnO and SiO_2 nanoparticles, respectively. The larger the K_L value, the greater the affinity between the absorbent and adsorbate molecules. From the results, Pb(II) has a greater affinity for all the nanoadsorbents used than Cd(II).[93] Additionally, the adsorption of Pb(II) onto ZnO/SiO_2 was more favorable than the adsorption of Cd(II). The value of R_L obtained for both Pb(II) and Cd(II) was less than 1, indicating the favorability of the adsorption process. The $1/n$ value for the Freundlich isotherm model ranges from 0.067 to 0.084 and the greater the interaction between adsorbent and adsorbate, the smaller the value of $1/n$.[94] The D-R isotherm model was used to differentiate between the physical and chemical adsorption of metal ions. The adsorption process is physical if the free energy of adsorption (E) is between 1 and 16 kJ mol^{-1} and is chemisorption if E is greater than 16 kJ mol^{-1}.[95] For all nanoadsorbents and metal ions, the E value determined in this research is larger than 16 kJ mol^{-1}. This shows that Pb(II) and Cd(II) adsorption is a chemisorption process. This result is similar to the earlier result obtained for thermodynamic and the kinetics studies where both Pb(II) and Cd(II) show a positive enthalpy value irrespective of the adsorbent used.

Adsorption kinetics

The nature of adsorption that occurs on the adsorbent surface was evaluated using various kinetic models, namely the pseudo-first-order, pseudo-second-order, intraparticle diffusion and Elovich kinetic models, and the findings are summarized in Table 5.

Table 5 indicates that the adsorption process conformed better to the pseudo-second-order kinetic model for both Pb(II) (R^2 = 0.863, 0.753 and 0.881) and Cd(II) (R^2 = 0.954, 0.953 and 0.996) than to first-order kinetics for all the nanoadsorbents with Pb(II) (R^2 = 0.990, 0.921 and 0.954) and Cd(II) (R^2 = 0.987, 0.953 and 0.996).

The data were also subjected to an error function analysis to determine the kinetics models' appropriateness. Table 5 reveals that the adsorption process predominantly followed the pseudo-second-order kinetic model, as demonstrated by lower x^2 and SSE values for both Pb(II) and Cd(II) when compared to the pseudo-first-order kinetic model. This finding supported the previous conclusion from the regression analysis (R^2) that the removal of Pb(II) and Cd(II) using ZnO and SiO_2 nanoparticles and ZnO/SiO_2 nanorods favored pseudo-second-order kinetics over pseudo-first-order kinetics. The pseudo-second-order kinetic model of adsorption implies that the rate-determining step of the adsorption process involves chemisorption (chemical reaction). To further understand the nature of the adsorption between adsorbent and adsorbate, the experimental data were subjected to the Elovich kinetic models (Table 5). The results also suggest that the adsorption of Pb(II) from refinery wastewater was greater than that of Cd(II) due to the higher value of R^2 for all nanoadsorbents. This indicates that the adsorption of Pb(II) and Cd(II) on the nanocomposites was more of chemical bonding than van der Waals forces. The adsorption process was also investigated by subjecting the data to the intraparticle diffusion model. The result (R^2) shows that intraparticle diffusion plays more of a role in the adsorption of Cd(II) ions for ZnO/SiO_2 nanorods compared to

Table 7. Comparison of removal of Pb(II) and Cd(II) ions using various nanoparticles and nanocomposites

Nanomaterial	Removal efficiency (%)	Metal ion	Experimental conditions	Best fit kinetics/ isotherm	Type of wastewater	Ref.
Polyaniline/ZnO	46	Cd(II)	0.1 g L^{-1} and at 25 °C after 400 min	Pseudo-second order/Langmuir isotherm	Industrial wastewater	98
ZnO/polymer	97.1, 80.9	Pb(II), Cd(II)	Dosage: 0.250 g; contact time: 60 min; metal ion concentration: 0.01 mol L^{-1}; temperature: 30 °C; time: 10 min	Pseudo-second order/Langmuir isotherm	Simulated wastewater	19
ZnO	89.2, 87.6 and 85.3	Cd(II), Pb(II)	Concentration (25 mg L^{-1})	Pseudo-second-order kinetic model		99
ZnO	93	Cd(II)	Temperature (30 °C), contact time (150 min), adsorbent dose (0.1 g), stirring speed (120 rpm)	Pseudo-second order/Langmuir isotherm	Simulated wastewater	100
ZnO/ montmorillonite	97.2	Pb(II)	Initial concentration (100 mg L^{-1}), contact time (2 h)	Pseudo-second order/Langmuir isotherm	Simulated wastewater	101
ZnO	98.00	Cd(II)	Contact time (40 min) at pH 3, adsorbent dosage (0.08 g)	Pseudo-second order/Temkin and Freundlich isotherms	Simulated wastewater	20
Casein/ZnO_2	95.35, 85.63	Pb(II), Cd(II)	Temperature (30 °C), adsorbent dosage (0.08 g), contact time (120 min), stirring speed (200 rpm)	Pseudo-second order/Langmuir isotherm	Simulated wastewater	102
$Cu_{0.5}Mg_{0.5}Fe_2O_4$	98.5	Pb(II)	pH (8.5), dosage (0.1 g), stirring speed (100 rpm), concentration (200 ppm), contact time (60 min)	Pseudo-second order	Simulated wastewater	103
ZnO_2/GO	56.81	Pb(II)	Dosage (0.16 g L^{-1}), pH (5), temperature (30 °C), time (30 min)	Pseudo-first order/ Langmuir isotherm	Simulated wastewater	104
Aminopropyl-functionalized silica	95		pH (9), temperature (30 °C)	—		105
Ash/GO/Fe_3O_4	99.67 and 98.68	Pb(II), Cd (II)	pH (6), concentration (10 mg L^{-1}), dosage (1 g), stirring speed (600 rpm), temperature (25 °C), contact time (150 min)	Pseudo-second order/Langmuir isotherm	Simulated wastewater	106
ZnO_2	80.00, 76.48	Pb(II), Cd (II)	Temperature (30 °C), stirring speed (250 rpm), contact time (15 min), dosage (0.08 g)	Pseudo-second order/Langmuir isotherm	Real industrial wastewater	This study
SiO_2	74.25, 70.99	Pb(II), Cd (II)	Temperature (30 °C), stirring speed (250 rpm), contact time (15 min), dosage (0.08 g)	Pseudo-second order/Langmuir isotherm	Real industrial wastewater	This study
ZnO/SiO_2	85.06, 84.12	Pb(II), Cd(II)	Temperature (30 °C), stirring speed (250 rpm), contact time (15 min), dosage (0.08 g)	Pseudo-second order/Langmuir isotherm	Real industrial wastewater	This study

Pb(II). The value of R^2 for all the kinetic models shows that the process of adsorption of Pb(II) and Cd(II) on the metal adsorbent used involves more than one mechanism, with chemical adsorption dominating the process.

Thermodynamic evaluation of adsorption process

The adsorption of Pd(II) and Cd(II) from petrochemical refinery wastewater using ZnO, SiO_2 and ZnO/SiO_2 nanorods was studied from a thermodynamic perspective to predict the adsorption mechanism. The slope and intercept of a linear plot of ln K_d *versus* 1/T were used to determine ΔH° and ΔS°, respectively (see Eqn 15). Standard Gibbs free energy change (ΔG°) was calculated using Eqn (16). The results are presented in Table 6.

$$\Delta G^\circ = -RT\ln K_d \tag{14}$$

$$\ln K_d = \frac{\Delta S}{R} - \frac{\Delta S}{RT} \tag{15}$$

$$\Delta G = \Delta H - T\Delta S \tag{16}$$

The positive values of ΔH° for Pb(II) and Cd(II) adsorption irrespective of the nanoadsorbents at an interval of temperatures confirmed that the adsorption process is endothermic. Many

researchers have observed similar findings, including Khezamia *et al*.[96] who studied the adsorption of Cd(II) by ZnO nanoparticles. The results in Table 6 suggest that $\Delta S°$ is positive irrespective of the adsorbent. This suggests higher randomness at the solid–solution interface, which could lead to a change in adsorbent and adsorbate structure. The change in Gibbs free energy ($\Delta G°$) showed a general decrease as the temperature increases as presented in Table 6. The positive $\Delta G°$ implies that the removal process needs more energy from external sources.[97]

The obtained maximum adsorption removal efficiency for the uptake of Pb(II) and Cd(II) onto ZnO and SiO_2 nanoparticles and ZnO/SiO_2 nanorods has been compared with the adsorptive capacity for other adsorbents available in the literature (Table 7).

The adsorption efficiency of Pb(II) and Cd(II) on ZnO and SiO_2 nanoparticles and ZnO/SiO_2 nanocomposites is lower, as evident from Table 7. This is not surprising because other authors used stimulated wastewater which has a higher concentration of metal ions compared to real industrial wastewater. Additionally, the lower adsorption efficiency compared to the other studies may also be linked to the presence of other pollutants in petrochemical wastewater, which usually compete for the active sites with the heavy metal ions against the use of stimulated wastewater that contained only the heavy metals. The differences in the adsorptive performance of the nanomaterials may also be ascribed to the applied experimental conditions. Maximum removal efficiency occurred within 15 min in this study compared to 30 min to 2 h reported in the literature (Table 7).

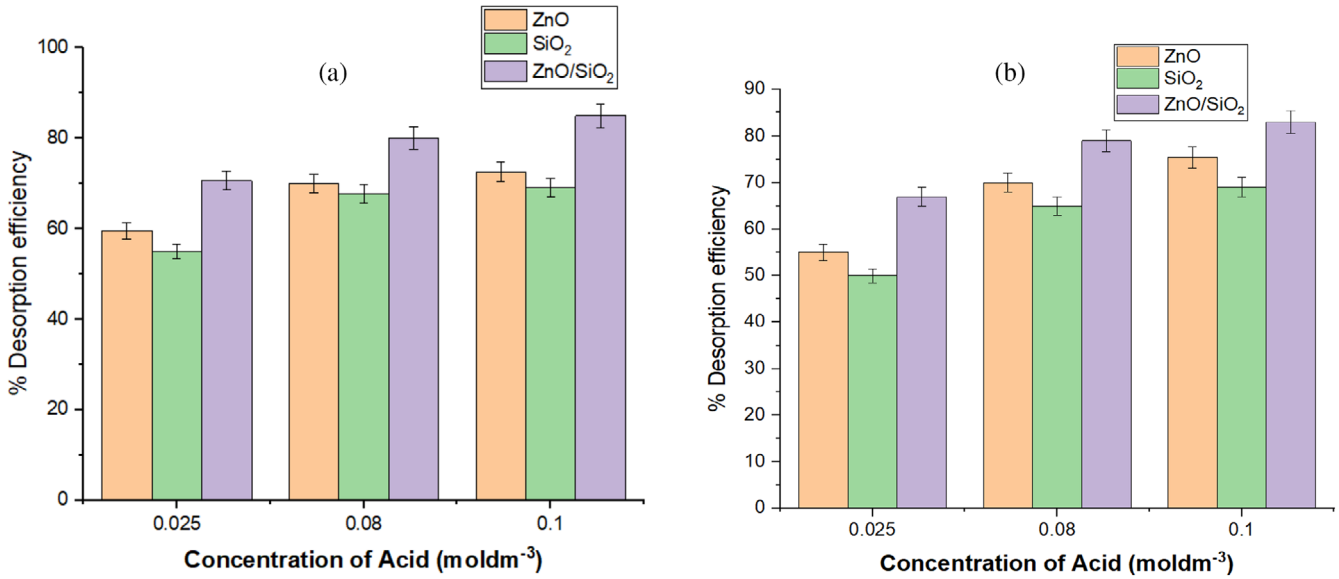

Figure 12. Effect of HNO_3 concentration on desorption efficiency of ZnO and SiO_2 nanoparticles and ZnO/SiO_2 nanocomposite for (a) Pb(II) and (b) Cd(II).

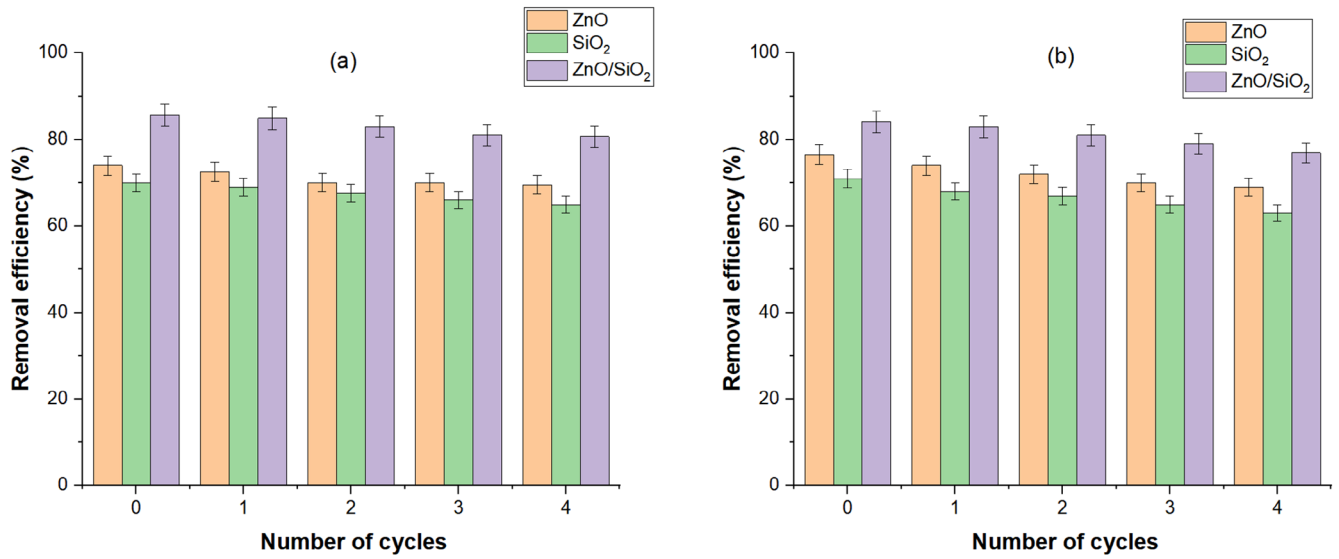

Figure 13. Desorption–adsorption of ZnO and SiO_2 nanoparticles and ZnO/SiO_2 nanocomposite for (a) Pb(II) and (b) Cd(II) after four cycles using 0.1 mol L^{-1} HNO_3 solution as the desorption agent.

Desorption and regeneration

Desorption

Desorption tests were carried out using ZnO and SiO_2 nanoparticles and ZnO/SiO_2 nanocomposites to determine the best concentration of HNO_3 to use in subsequent regeneration cycles. The results are presented in Fig. 12.

Figure 12 shows that the desorption of both Pb(II) and Cd(II) increases as the concentration of nitric acid increases from 0.025 to 0.05 and 0.1 mol L^{-1} for ZnO and SiO_2 nanoparticles and ZnO/SiO_2 nanocomposites. The result in Fig. 12(a) suggests that Pb(II) recovery of 72.541%, 69.00% and 83.931% was achieved. Figure 12(b) demonstrates that the highest Cd(II) recovery from the surface of ZnO and SiO_2 nanoparticles and ZnO/SiO_2 nanocomposites was 75.34%, 69.07% and 82.98% at a desorption time of 15 min, dosage of 0.05 g and temperature of 35 °C. The findings indicated that 0.1 mol L^{-1} of HNO_3 led to recovery of more metal ions than 0.025 and 0.05 mol L^{-1} irrespective of the adsorbent used. This may be ascribed to the fact that an increase in the concentration of HNO_3 caused increases in the number of H^+ in solution, which increases the concentration gradient of the metal ions and H^+ and therefore increases the driving force for ion exchange, which favored metal ions during the desorption process.[107] The results in this study corroborate the analysis of Bayuo *et al.*[108] who reported similar values using 0.1 mol L^{-1} H_2SO_4 (82.1%) and HCl (74.2%) for desorption of Pb(II). Similar results have been reported by Samson *et al.*,[109] who studied desorption using different concentrations of HCl (0.01, 0.1, 1.0 and 1.20 mol L^{-1}). Those authors reported a desorption efficiency of 68% at 0.3 mol L^{-1}. This result confirms that an increase in the concentration of acid increases the desorption of heavy metals. However, it has been reported that a higher concentration of acid above 0.15 mol L^{-1} may damage the structure of the adsorbent.[28]

Regeneration

Regeneration of an adsorbent is a significant aspect in increasing the efficiency of the adsorption process and can lower operating costs while also protecting the environment.[110] Adsorption–desorption cycles of Pb(II) and Cd(II) were conducted four times using ZnO and SiO_2 nanoparticles and ZnO/SiO_2 nanocomposites. The results are presented in Fig. 13.

Figure 13(a) demonstrates that the adsorption removal efficiency of Pb(II) onto ZnO and SiO_2 nanoparticles and ZnO/SiO_2 nanocomposites was 69.54%, 65.95% and 80.651% while the values obtained for Cd(II) (Fig. 13(b)) were 69.00%, 63.89% and 76.907% after four cycles. Generally, the desorption–adsorption result for both Pb(II) and Cd(II) remained consistent after four cycles with no significant differences. The high adsorption efficiency of the nanoparticles could be explained by the fact that the use of an acid as a desorbing agent increases the adsorption properties of the adsorbent.[111] It has been found that if the spent adsorbent can be regenerated and utilized again after the first cycle, the adsorbent is considered to be cost-effective and economically viable.[112] The adsorbent used in this work showed high removal efficiency even after four adsorption–desorption cycles, suggesting that the adsorbent provides an economic benefit by being able to be reused in the removal of Pb(II)and Cd(II) via adsorption processes. Generally, ZnO/SiO_2 nanocomposites were very stable compared with ZnO and SiO_2 nanoparticles. As a result, it is possible to conclude that ZnO/SiO_2 nanocomposites are stable and reusable and that they could be used multiple times to remove heavy metals such as Pb(II) and Cd(II) from wastewater.

CONCLUSIONS

The applicability of ZnO and SiO_2 nanoparticles and ZnO/SiO_2 nanorods was studied as new adsorbents for the removal of Pb(II) and Cd(II) from refinery wastewater. The batch studies demonstrated that the adsorption process was controlled by contact time, adsorbent dosage and reaction temperature. ZnO/SiO_2 composites performed better as an nanoadsorbent for the removal of Pb(II) and Cd(II) ions from refinery wastewater than ZnO nanoparticles and SiO_2 nanoparticles. The results showed that the ZnO/SiO_2 nanorods had the highest removal of 85.06% and 84.12% for Pb(II) and Cd(II) ions. The adsorption of Pb(II) and Cd(II) onto the ZnO/SiO_2 nanorods was endothermic and feasible at a higher temperature. The adsorption process fits pseudo-second-order kinetics. Physicochemical adsorption was identified to be the nature of the adsorption rather than the purely physical and chemical adsorption, though chemical adsorption dominated. The adsorption process fits better the Langmuir isotherm with maximum adsorption capacity of 30.772, 24.860 and 37.951 mg g^{-1} for Pb(II) and 30.328, 20.124 and 33.603 mg g^{-1} for Cd(II) using ZnO and SiO_2 nanoparticles and ZnO/SiO_2 nanocomposite as adsorbents.

Four desorption–adsorption cycles were conducted. The ZnO/SiO_2 nanocomposite was more stable than ZnO and SiO_2 with removal of 80.651% and 76.907% for Pb(II) and Cd(II) after four desorption–adsorption cycles under conditions of desorption concentration of 0.1 mol L^{-1} NHO_3, time of 15 min, dosage of 0.05 g and temperature of 35 °C. The desorption–adsorption cycles revealed that the ZnO/SiO_2 nanocomposites were more stable than ZnO and SiO_2 nanoparticles, indicating that the ZnO/SiO_2 nanocomposites were better and more economical compared to ZnO and SiO_2 nanoparticles and they can be reused.

FUNDING INFORMATION

The authors declare that no funds, grants or other support were received during the preparation of this paper.

CONFLICT OF INTEREST

The authors have no relevant financial or non-financial interests to disclose.

AUTHOR CONTRIBUTIONS

All authors contributed to the study conception and design. Material preparation, data collection and analysis were performed by EYS, JOT, JOJ and MATS. The first draft of the manuscript was written by EYS and all authors commented on previous versions of the manuscript. All authors read and approved the final manuscript.

ACKNOWLEDGEMENTS

The authors appreciate the contributions of technical assistance of the following people: Dr. Remy Bucher (XRD analysis, iThemba Labs, South Africa); Dr. Franscious Cummings (HRSEM/HRTEM/SAED/EDS) analysis, Physics Department, University of the Western Cape (UWC), South Africa; Prof. WD Roos (XPS analysis); Mr. Sandeeran Govender (BET analysis), Chemical Engineering Department, University of Cape Town, South Africa.

SUPPORTING INFORMATION

Supporting information may be found in the online version of this article.

REFERENCES

1 Rahi MN, Jaeel AJ and Abbas AJ, Treatment of petroleum refinery effluents and wastewater in Iraq: a mini review. *IOP Conf Ser* **1058**: 12–72 (2021).
2 Mohammadi L, Rahdar A, Bazrafshan E, Dahmardeh H, Susan MAB and Kyzas GZ, Petroleum hydrocarbon removal from wastewaters: a review. *Processes* **8**:447–645 (2020).
3 Mohanakrishna G, Abu-Reesh IM and Pant D, Enhanced bioelectrochemical treatment of petroleum refinery wastewater with Labaneh whey as co-substrate. *Sci Rep* **10**:1–11 (2020).
4 Briffa J, Sinagra E and Blundell R, Heavy metal pollution in the environment and their toxicological effects on humans. *Heliyon* **9**:1–20 (2020).
5 Balali-Mood M, Naseri K, Tahergorabi Z, Khazdair MR and Sadeghi M, Toxic mechanisms of five heavy metals: mercury, lead, chromium, cadmium and arsenic. *Front Pharmacol* **12**:643–972 (2021).
6 Wilk A, Romanowski M and Wiszniewska B, Analysis of cadmium, mercury and lead concentrations in erythrocytes of renal transplant recipients from northwestern Poland. *Biology* **10**:1–11 (2021).
7 Obasi PN and Akudinobi BB, Potential health risk and levels of heavy metals in water resources of lead–zinc mining communities of Abakaliki, Southeast Nigeria. *Appl Water Sci* **10**:1–23 (2020).
8 Wang Y, Leilei L, Luo C and Duan H, Removal of Pb(II) from water environment using a novel magnetic chitosan/graphene oxide imprinted Pb(II). *Int J Bio Macro* **86**:505–511 (2016).
9 Palani G, Arputhalatha A, Kannan K, Lakkaboyana SK, Hanafiah MM, Kumar V *et al*., Current trends in the application of nanomaterials for the removal of pollutants from industrial wastewater treatment: a review. *Molecules* **26**:1–16 (2021).
10 Qasem NAA, Mohammed RH and Lawal DU, Removal of heavy metal ions from wastewater: a comprehensive and critical review. *Clean Water* **4**:1–36 (2021).
11 Schneider A, Herlevi LM, Guo Y and Lahore HMZ, Perspectives on adsorption technology as an effective strategy for continuous downstream bioprocessing. *J Chem Technol Biotechnol* **52**:1–41 (2021).
12 Liang S, Li Y, Qu G, Yang C, Yang C and Zhou J, Preparation of recyclable materials for removing heavy metal ions in aqueous solution and wastewater applications. *J Chem Technol Biotechnol* **12**:1–26 (2021).
13 Saleem J, Shahid U, Hijab M, Mackey H and McKay G, Production and applications of activated carbons as adsorbents from olive stones. *Biomass Conv Bioref* **9**:775–802 (2019).
14 Andrade RGD, Veloso SR, Castanheira S and Elisabete MS, Shape anisotropic iron oxide-based magnetic nanoparticles: synthesis and biomedical applications. *Int J Mol Sci* **21**:2455–5433 (2020).
15 Aragaw TA, Bogale FM and Aragaw BA, Iron-based nanoparticles in wastewater treatment: a review on synthesis methods applications and removal mechanisms. *J Saud Chem Soc* **25**:101–280 (2021).
16 Tan WK, Muto H, Kawamura G, Lockman Z and Matsuda A, Nanomaterial fabrication through the modification of sol–gel derived coatings. *Nanomaterials* **11**:181 (2021).
17 Shaba EY, Jacob JO, Tijani JO and Suleiman MAT, A critical review of synthesis parameters affecting the properties of zinc oxide nanoparticle and its application in wastewater treatment. *Appl Water Sci* **11**: 1–42 (2021).
18 Gegova-Dzhurkova R, Nesheva D, Dzhurkov V, Šćepanović M, Grujić-Brojčin M, Bineva I *et al*., Modification of surface morphology and lattice order in nanocrystalline ZnO thin films prepared by spin-coating sol–gel method. *J Sol-Gel Sci Technol* **100**:55–67 (2021).
19 Angelin KB, Siva S and Kannan RS, Zinc oxide nanoparticles impregnated polymer hybrids for efficient extraction of heavy metals from polluted aqueous solution. *Asian J Sci Technol* **6**:2139–2150 (2015).
20 Kamath S, Gopal V, Ramanjaneyalu V and Kamila S, Application of ZnO nano rods for the batch adsorption of Cr(VI): a study of kinetics and isotherms. *Am J Appl Sci* **16**:1–12 (2018).
21 Joshi NC, Malik S and Gururani P, Utilization of polypyrrole/ZnO nanocomposite in the adsorptive removal of Cu^{2+}, Pb^{2+} and Cd^{2+} ions from wastewater. *Lett ApplNanoBioScience* **10**:2339–2351 (2021).
22 Tho PT, Van HT, Nguyen LH, Hoang TK, Tran TN, Nguyen TT *et al*., Enhanced simultaneous adsorption of As(III), Cd(II), Pb(II) and Cr(VI) ions from aqueous solution using cassava root husk-derived biochar loaded with ZnO nanoparticles. *RSC Adv* **11**:18881–18897 (2021).
23 Rastegari E, Hsiao YJ, Lai WY, Lai YH, Yang TC, Chen SJ *et al*., An update on mesoporous silica nanoparticle applications in nanomedicine. *Pharmaceutics* **13**:1067 (2021).
24 Sheet I, Kabbani A and Holail H, Removal of heavy metals using nanostructured graphite oxide silica nanoparticles and silica/ graphite oxide composite. *Energy Procedia* **50**:130–138 (2014).
25 Soltani RDC, Khoramabadi GS, Godini H and Noorimotlagh Z, The application of ZnO/SiO_2 nanocomposite for the photocatalytic degradation of a textile dye in aqueous solutions in comparison with pure ZnO nanoparticles. *Desalination Water Treat* **56**:2551–2558 (2015).
26 Babu KL, Rao SH, Kishore PNR and Reddy RYV, Hydrothermal synthesis of flower-like $ZnO\text{-}SiO_2$ nanocomposites for solar light-induced photocatalysis and anti-bacterial applications. *Mater Res Express* **52**:1–24 (2019).
27 Bayuo J, Abukari MA and Pelig-Ba KB, Desorption of chromium(VI) and lead(II) ions and regeneration of the exhausted adsorbent. *Appl Water Sci* **10**:1–6 (2020). https://doi.org/10.1007/s13201-020-01250-y.
28 Pate H, Elution profile of cationic and anionic adsorbate from exhausted adsorbent using solvent desorption. *Sci Rep* **12**:1–11 (2022).
29 Bokov D, Jalil AT, Chupradit S, Suksatan W, Ansari MJ, Shewael IH *et al*., Nanomaterial by sol-gel method: synthesis and application. *Adv Mater Sci Eng* **9**:1–21 (2022).
30 Turek A, Wieczorek K and Wolf WM, Digestion procedure and determination of heavy metals in sewage sludge: an analytical problem. *Sustainability* **11**:1–10 (2019).
31 Edokpayi O, Osemwenkhae O, Ayodele BV, Ossai J, Fadilat SA and Ogbeide SE, Batch adsorption study of methylene blue in aqueous solution using activated carbons from rice husk and coconut Shell. *J Appl Sci Environ Manage* **22**:631–635 (2018).
32 Lata S, Singh PK and Amadder SR, Regeneration of adsorbents and recovery of heavy metals: a review. *Int J Environ Sci Technol* **12**: 1461–1478 (2019).
33 Hubbe MA, Azizian S and Douven S, Implications of apparent pseudo-second-order adsorption kinetics onto cellulosic materials: a review. *BioRes* **14**:7582–7626 (2019).
34 Jasper EE, Ajibola VO and Onwuka JC, Nonlinear regression analysis of the sorption of crystal violet and methylene blue from aqueous solutions onto an agro-waste derived activated carbon. *Appl Water Sci* **10**:1–11 (2020).
35 Marczewski AW, Seczkowska M and Deryło-Marczewska A, Adsorption equilibrium and kinetics of selected phenoxyacid pesticides on activated carbon: effect of temperature. *Adsorption* **22**:777–790 (2016).
36 Musah M, Yisa J, Suleiman T, Mann A, Shaba EY, Aliyu A, Kinetics and isotherms studies of the adsorption of Cr^{6+}, Mn^{2+} and Cd^{2+} ions onto chemically modified bombax *Buonopozense calyx* **15**:1–7 (2018).
37 Pholosi A, Naidoo EB and Ofomaja AE, Intraparticle diffusion of Cr(VI) through biomass and magnetite coated biomass: a comparative kinetic and diffusion study. *South Afr J Chem Eng* **32**:39–55 (2020).
38 Zeldowitsch J, Über den mechanismus der katalytischen oxydation von CO an MnO_2. *Acta Physicochem URSS* **1**:364–449 (1934).
39 Adeogun AI and Balakrishnan RB, Kinetics isothermal and thermodynamics studies of electrocoagulation removal of basic dye rhodamine B from aqueous solution using steel electrodes. *Appl Water Sci* **7**:1711–1723 (2017).
40 Ahmad NH, Mohamed MA and Yusoff FM, Improved adsorption performance of rubber-based hydrogel: optimisation through response surface methodology isotherm and kinetic studies. *J Sol-G Sci Technol* **1-13**:322–334 (2020).
41 Shrestha B, Wang L, Zhang H, Hung CY and Tang L, Gold nanoparticles mediated drug-gene combinational therapy for breast cancer treatment. *Int J Nanomed* **15**:8109–8119 (2020).
42 Widiyastuti W, Machmudah S, Nurtono T, Winardi S and Okuyama K, Synthesis of $ZnO\text{-}SiO_2$ nanocomposite particles and their characterization by sonochemical method. *AIP Conference Proceedings International Seminar on Fundamental and Application of Chemical Engineering 2016 (ISFAChE 2016)*, 1–10 (2017).
43 Abello-Ribota BS, Farías R and Reyes-López SY, Surface enhanced infrared absorption studies of SiO_2–TiO_2–Ag nanofibers: effect of

silver electrodeposition time on the amplification of signals. *Crystals* **11**:563 (2021).
44 Paulish AG, Dmitriev AK and Gelfand AV, Absorption spectral characteristics of infrared radiation in silicon dioxide films for thermal radiation detectors. *Optoelectron Instrum Proc* **55**:508–512 (2019).
45 Vinoda BM, Vinuth M, Bodke YD and Manjanna J, Photocatalytic degradation of toxic methyl red dye using silica nanoparticles synthesized from rice husk ash. *J Environ Anal Toxicol* **5**:336 (2015).
46 Jimenéz-Vivanco MR, García G, Carrillo J, Agarwal V, Díaz-Becerril T, Doti R *et al*., Porous Si-SiO_2 based UV microcavities. *Sci Rep* **10**:1–21 (2020).
47 Gao Y, Zhong D, Zhang D, Pu X, Shao X, Su C *et al*., Thermal regeneration of recyclable reduced graphene oxide/Fe_3O_4 composites with improved adsorption properties. *J Chem Technol Biotechnol* **89**:1859–1865 (2014).
48 Valle AL, Silva ACA and Dantas NO, Sabino-Silva R Melo FCC, Moreira CS and Goulart LR, Application of ZnO nanocrystals as a surface-enhancer FTIR for glyphosate detection. *Nanomaterials* **11**:509 (2021).
49 Quadri TW, Olasunkanmi LO, Fayemi OE, Solomon MM and Ebenso EE, Zinc oxide nanocomposites of selected polymers: synthesis characterization and corrosion inhibition studies on mild steel in HCl solution. *ACS Omega* **2**:8421–8437 (2017).
50 Nguyen NT, Nguyen NT and Nguyen VA, In situ synthesis and characterization of ZnO/chitosan nanocomposite as an adsorbent for removal of Congo red from aqueous solution. *Adv Polym Technol* **1–8**:3892694 (2020).
51 Chen Y, Ding H and Sun S, Preparation and characterization of ZnO nanoparticles supported on amorphous SiO_2. *Nanomaterials* **7**:217 (2017).
52 Ahmad KS and Jaffri SB, Phytosynthetic ag doped ZnO nanoparticles: semiconducting green remediators: photocatalytic and antimicrobial potential of green nanoparticles. *Open Chem* **16**:556–570 (2019).
53 Noukelag SK, Mohamed HEA, Moussa B, Razanamahandry LC, Ntwampe SKO, Arendse CJ *et al*., Investigation of structural and optical properties of biosynthesized zincite (ZnO) nanoparticles (NPs) via an aqueous extract of *Rosmarinus officinalis* (rosemary) leaves. *MRS Adv* **1–10**:2349–2358 (2020).
54 Rahmat F, Fen YW, Anuar MF, Omar NAS, Zaid MHM, Matori KA *et al*., Synthesis and characterization of ZnO-SiO_2 composite using oil palm empty fruit bunch as a potential silica source. *Molecules* **26**:1–10 (2021).
55 Mohammed AJ and Sabbar KW, Structural and morphological studies for ZnO:SnO_2 composite thin films. *Int J Enhanc Res Sci Technol Eng* **2**:45–55 (2018).
56 Huang XJ, Zeng XF, Wang JX, Zhang LL and Chen JF, Synthesis of monodispersed ZnO@SiO_2 nanoparticles for anti-UV aging application in highly transparent polymer-based nanocomposites. *J Mater Sci* **54**:8581–8590 (2019).
57 Al-Tayyar NA, Youssef AM and Al-Hindi RR, Antimicrobial packaging efficiency of ZnO-SiO_2 nanocomposites infused into PVA/CS film for enhancing the shelf life of food products. *Food Packag Shelf Life* **25**:100–523 (2020).
58 Bahrami K and Karami Z, Core/shell structured ZnO@SiO_2 TTIP composite nanoparticles as an effective catalyst for the synthesis of 2-substituted benzimidazoles and benzothiazoles. *J Exp Nanosci* **13**:272–283 (2018).
59 Pereira FJ, Díez MT and Aller AJ, Effect of temperature on the crystallinity size and fluorescent properties of zirconia-based nanoparticles. *Mater Chem Phys* **152**:135–146 (2015).
60 Zenkovets GA, Shutilov AA, Bondareva VM, Sobolev VI, Marchuk A, Tsybulya SV *et al*., New multicomponent MoVSbNbCeOx/SiO_2 catalyst with enhanced catalytic activity for oxidative dehydrogenation of ethane to ethylene. *ChemCatChem* **12**:1–16 (2020).
61 Chen G, Wang T, Li C, Yang L, Xu T, Zhu W *et al*., Enhanced photovoltaic performance in inverted polymer solar cells using Li ion doped ZnO cathode buffer layer. *Org Electron* **36**:50–56 (2016).
62 Claros M, Setka M, Jimenez YP and Vallejos S, Aacvd synthesis and characterization of iron and copper oxides modified ZnO structured films. *Nanomaterials* **10**:471–497 (2020).
63 Chen G, Liu F, Ling Z, Zhang P, Wei B and Zhu W, Efficient organic light emitting diodes using solution-processed alkali metal carbonate doped ZnO as electron injection layer. *Front Chem* **7**:226 (2019).
64 Yahmadi B, Kamoun O, Alhalaili B, Alleg S, Vidu R and Kamoun TN, Physical investigations of (Co,Mn) co-doped ZnO nanocrystalline films. *Nanomaterials* **10**:1–13 (2020).
65 Jilani A, Iqbal J, Abdel-Wahab MS, Jamil Y and Al-Ghamdi AA, X-ray photoelectron spectroscopic (XPS) investigation of interface diffusion of ZnO/Cu/ZnO multilayer. *J Optoelectr Biomed Mater* **8**:1–27 (2016).
66 Gao YK, Traeger F, Shekha O, Idriss H and Wöll C, Probing the interaction of the amino acid alanine with the surface of ZnO. *J Colloid Interface Sci* **338**:16–21 (2009).
67 Bourlier Y, Frégnaux M, Bérini B, Fouchet A, Dumont Y and Aureau D, XPS monitoring of $SrVO_3$ thin films from demixing to air ageing: the asset of treatment in water. *Appl Surf Sci* **553**:149536 (2021).
68 Chang FM, Brahma S, Huang JH, Wu ZZ and Lo KY, Strong correlation between optical properties and mechanism in deficiency of normalized self-assembly ZnO Nanorods. *Sci Rep* **9**:1–9 (2019).
69 Barnett CJ, Navarro-Torres J, McGettrick JD, Maffeis TGG and Barron RA, Inducing upwards band bending by surface stripping ZnO nanowires with argon bombardment. *Nanotechnology* **31**:1–7 (2020).
70 Nguyen T, Valle N, Guillot J, Bour J, Adjeroud N, Fleming Y *et al*., Elucidating the growth mechanism of ZnO films by atomic layer deposition with oxygen gas via isotopic tracking. *J Mater Chem C* **9**:4307–4315 (2022).
71 Agboola O, Fayomi OSI, Ayodeji A, Ayeni AO, Alagbe, EE, Sanni SE, *et al*., Review on polymer nanocomposites and their effective applications in membranes and adsorbents for water treatment and gas Separation. *Membranes* **139**, 1–36 (2021). https://doi.org/10.3390/membranes11020139.
72 Oliveira JCA, Galdino AL, Gonçalves DV, Silvino PFG, Cavalcante CL, Bastos-Neto M *et al*., Representative pores: an efficient method to characterize activated carbons. *Front Chem* **8**:1265 (2021).
73 EPA, pH Overview. Available: https://www.epa.gov/caddis-vol2/caddis-volume-2-sources-stressors-responses-ph [15 March 2022].
74 Zhou R, Ma X, Li H, Sun C and Bai B, Specific heat capacity of confined water in extremely narrow graphene nanochannels. *Front Energy Res* **1**:1–21 (2021).
75 WHO (2017). Guidelines for drinking-water quality, 4th edition incorporating the 1st addendum. Available: https://www.who.int/publications/i/item/9789241549950 [13 February 2022].
76 Xu J, Jin GM, Yuming T and Hongwu LL, Assessing anthropogenic impacts on chemical and biochemical oxygen demand in different spatial scales with bayesian networks. *Water* **12**:1–19 (2020).
77 Virgen MRM, Vázquez OFA, Hernández V, Montoya HV, Gómez RT (2018). Removal of heavy metals using adsorption processes subject to an external magnetic field. IntechOpen DOI: 10.5772/intechopen.74050. Available: https://www.intechopen.com/books/heavy-metals/removal-of-heavy-metals-using-adsorption-processes-subject-to-an-external-magnetic-field [10 January 2022].
78 Andronic L, Perniu D and Duta A, Synergistic effect between TiO_2 sol-gel and Degussa P25 in dye photodegradation. *Sol-Gel Sci Technol* **66**:472–480 (2013).
79 El-Saied FA, Abo-Elenan SA and El-shinawy FH, Removal of lead and copper ions from polluted aqueous solutions using nano sawdust particles. *Int J Waste Resour* **7**:305 (2017).
80 Fan X, Liu H, Anang E and Ren D, Effects of electronegativity and hydration energy on the selective adsorption of heavy metal ions by synthetic NaX zeolite. *Materials* **14**:1–16 (2021).
81 Li X, He S, Feng C, Zhu Y, Pang Y, Hou J *et al*., Non-competitive and competitive adsorption of Pb(II) and Zn^{2+} ions onto SDS in process of micellar-enhanced ultrafiltration. *Sustainability* **10**:1–12 (2018).
82 Rodríguez C, Tapia C, Leiva-Aravena E and Leiva E, Graphene oxide–ZnO nanocomposites for removal of aluminum and copper ions from acid mine drainage wastewater. *Int J Environ Res Public Health* **17**:1–18 (2020).
83 Gisi S, Lofrano G, Grassi M and Notarnicola M, Characteristics and adsorption capacities of low-cost sorbents for wastewater treatment: a review. *Sustain Mater Technol* **9**:10–40 (2016).
84 Huang H, Wang Y, Zhang Y, Niu Z and Li X, Amino-functionalized graphene oxide for Cr(VI), Cu(II), Pb(II) and Cd(II) removal from industrial wastewater. *Open Chem* **18**:97–107 (2020).
85 Xie J, Lin Y, Li C, Wu D and Kong H, Removal and recovery of phosphate from water by activated aluminum oxide and lanthanum oxide. *Powder Technol* **269**:351–357 (2015).
86 Jiang LL, Yu HT, Pei LF and Hou XG, The effect of temperatures on the synergistic effect between a magnetic field and functionalized

graphene oxide-carbon nanotube composite for Pb(II) and phenol adsorption. *J Nanomater* **1**:1–13 (2018).
87 Jibril A, Jean M, Bada SW and Oboirien B, Equilibria and isosteric heat of adsorption of methane on activated carbons derived from South African coal discards. *ACS Omega* **5**:32530–32539 (2020).
88 Xu P, Zeng GM, Huang DL, Yan M, Chen M, Lai C *et al*., Fabrication of reduced glutathione functionalized iron oxide nanoparticles for magnetic removal of Pb(II) from wastewater. *J Taiwan Inst Chem Eng* **71**:165–173 (2017). https://doi.org/10.1016/j.jtice.2016.11.031.
89 Gebretsadik H, Gebrekidan A and Demlie L, Removal of heavy metals from aqueous solutions using *Eucalyptus camaldulensis*: an alternate low-cost adsorbent. *Cogent Chem* **6**:1–16 (2020).
90 Mouni L, Belkhiri L, Bollinger JC, Bouzaza A, Assadi A, Tirri A *et al*., Removal of methylene blue from aqueous solutions by adsorption on kaolin: kinetic and equilibrium studies. *Appl Clay Sci* **153**:38–45 (2018).
91 Edet UA and Ifelebuegu AO, Kinetics isotherms and thermodynamic modeling of the adsorption of phosphates from model wastewater using recycled brick waste. *Processes* **8**:1–15 (2020).
92 Sadegh H, Ali GAM, Gupta VK, Makhlouf ASH, Shahryari-ghoshekandi R, Nadagouda MN *et al*., The role of nanomaterials as effective adsorbents and their applications in wastewater treatment. *J Nanostruct Chem* **71–14**:1–14 (2017).
93 Adane B, Siraj K and Meka N, Kinetic equilibrium and thermodynamic study of 2-chlorophenol adsorption onto *Ricinus communis* pericarp activated carbon from aqueous solutions. *Green Chem Lett Rev* **8**:1–12 (2015).
94 Al-Ghouti MA and Al-Absi RS, Mechanistic understanding of the adsorption and thermodynamic aspects of cationic methylene blue dye onto cellulosic olive stones biomass from wastewater. *Sci Rep* **10**:1–18 (2020).
95 Ayawei N, Ebelegi AN and Wankasi D, Modelling and interpretation of adsorption isotherms. *J Chem* **11**:1–11 (2017).
96 Khezamia L, Kamal KT, Amamic E, Ghiloufid I and Mir LI, Removal of cadmium(II) from aqueous solution by zinc oxide nanoparticles: kinetic and thermodynamic studies. *Desalination Water Treat* **11**:1–11 (2016).
97 Osińska M, Removal of lead(II), copper(II), cobalt(II) and nickel(II) ions from aqueous solutions using carbon gels. *J Sol-Gel Sci Technol* **81**: 678–692 (2017).
98 Moosavian MA and Moazezi N, Removal of cadmium and zinc ions from industrial wastewater using nanocomposites of PANI/ZnO and PANI/CoHCF: a comparative study. *Desalination Water Treat* **1–20**:1–20 (2015).
99 Ciesielczyk F, Bartczak P and Jesionowski T, Removal of Cd(II) and Pb(II) ions from model aqueous solutions using sol–gel-derived inorganic oxide adsorbent. *Adsorption* **22**:445–458 (2016).
100 Anusa R, Ravichandran C and Sivakumar EK, Removal of heavy metal ions from industrial waste water by nano-ZnO in presence of electrogenerated Fenton's reagent. *Int J ChemTech Res* **10**:501–508 (2017).
101 Kamath S, Gopal V, Ramanjaneyalu V and Kamila S, Application of ZnO nano rods for the batch adsorption of Cr(VI): a study of kinetics and isotherms. *Am J Appl Sci* **16**:1–12 (2018).
102 Somu P and Paul S, Casein based biogenic-synthesized zinc oxide nanoparticles simultaneously decontaminate heavy metals dyes and pathogenic microbes: a rational strategy for wastewater treatment. *J Chem Technol Biotechnol* **93**:2962–2976 (2018). https://doi.org/10.1002/jctb.5655.
103 Tran CV, Quang DV, Thi HP, Truong TN and La DD, Effective removal of Pb(II) from aqueous media by a new design of Cu–Mg binary ferrite. *ACS Omega* **5**:7298–7306 (2020).
104 Ahmad SZN, Norharyat W, Salleh W, Yusof N, Yusop MZM, Hamdan R *et al*., Pb(II) removal and its adsorption from aqueous solution using zinc oxide/graphene oxide composite. *Chem Eng Commun* **208**:646–660 (2021).
105 Alswieleh AM, Albahar HY, Alfawaz AM, Alsilme AS, Beagan AM, Alsalme AM *et al*., Evaluation of the adsorption efficiency of glycine-, iminodiacetic acid- and amino propyl-functionalized silica nanoparticles for the removal of potentially toxic elements from contaminated water solution. *J Nanomater* **2021**:1–12 (2021).
106 Pelalak R, Heidari Z, Khatami SM, Kurniawan TA, Marjani A and Shirazian S, Oak wood ash/GO/Fe_3O_4 adsorption efficiencies for cadmium and lead removal from aqueous solution: kinetics equilibrium and thermodynamic evaluation. *Arab J Chem* **14**:1–15 (2021).
107 Xie J, Lin Y, Li C, Wu D and Kong H, Removal and recovery of phosphate from water by activated aluminum oxide and lanthanum oxide. *Powder Technol* **269**:351–357 (2015).
108 Bayuo J, Abukari MA and Pelig-Ba KB, Desorption of chromium(VI) and lead(II) ions and regeneration of the exhausted adsorbent. *Appl Water Sci* **10**:1–6 (2020). https://doi.org/10.1007/s13201-020-01250-y.
109 Samson O, Adedibu O and Tella C, Removal of hexavalent chromium from aqueous solutions by adsorption on modified groundnut hull. *Beni-Suef Univ J Basic Appl Sci* **5**:377–388 (2016).
110 Prajapati AK, Verma P, Singh S and Mondal MK, Adsorption-desorption surface bindings, kinetics, and mass transfer behavior of thermally and chemically treated great millet husk towards Cr(VI) removal from synthetic wastewater. *Adsorption Sci Technol* **1-6**:1–16 (2022).
111 Coltre DSC, Cionek CA, Meneguin JG, Maeda CH, MUC B, de Araújo AC *et al*., Study of dye desorption mechanism of bone char utilizing different regenerating agents. *SN Appl Sci* **2**:1–14 (2020). https://doi.org/10.1007/s42452-020-03911-8.
112 Indah S, Helard D and Binuwara A, Studies on desorption and regeneration of natural pumice for iron removal from aqueous solution. *Water Sci Technol* **2017**:509–515 (2018).

